

RING++: Roto-translation Invariant Gram for Global Localization on a Sparse Scan Map

Xuecheng Xu*, Sha Lu*, Jun Wu, Haojian Lu, Qiuguo Zhu, Yiyi Liao, Rong Xiong and Yue Wang

Abstract—Global localization plays a critical role in many robot applications. LiDAR-based global localization draws the community’s focus with its robustness against illumination and seasonal changes. To further improve the localization under large viewpoint differences, we propose RING++ which has roto-translation invariant representation for place recognition, and global convergence for both rotation and translation estimation. With the theoretical guarantee, RING++ is able to address the large viewpoint difference using a lightweight map with sparse scans. In addition, we derive sufficient conditions of feature extractors for the representation preserving the roto-translation invariance, making RING++ a framework applicable to generic multi-channel features. To the best of our knowledge, this is the first learning-free framework to address all subtasks of global localization in the sparse scan map. Validations on real-world datasets show that our approach demonstrates better performance than state-of-the-art learning-free methods, and competitive performance with learning-based methods. Finally, we integrate RING++ into a multi-robot/session SLAM system, performing its effectiveness in collaborative applications.

Index Terms—Global Localization, Place Recognition, Simultaneous Localization and Mapping.

I. INTRODUCTION

GLOBAL localization aims to estimate the pose of a robot in a map using onboard sensor measurements without priors. This task is essential for many robotics applications, including loop closures and map alignments in SLAM systems, and relocalization in navigation systems. Vision-based methods have advanced rapidly in the last decade by exploiting image cues. However, these approaches are sensitive to illumination and seasonal changes between current and mapping session [1], [2]. Recent studies have shown that LiDAR can be employed to overcome the difficulty [3]–[6]. However, even with LiDAR-based methods, reliable localization is still challenging when the current scan and mapping sessions have trajectories with large viewpoint differences.

To clarify the challenge, we define the global localization as a search problem: the query is the current LiDAR scan, and the search space is the pose space covering the entire map. A typical global localization pipeline consists of two steps: place recognition and pose estimation, solving the problem in a coarse-to-fine process. As shown in Fig. 1, these two steps are divided by the *place*, which encodes a representative scan and its pose. At the coarse level, the search space is

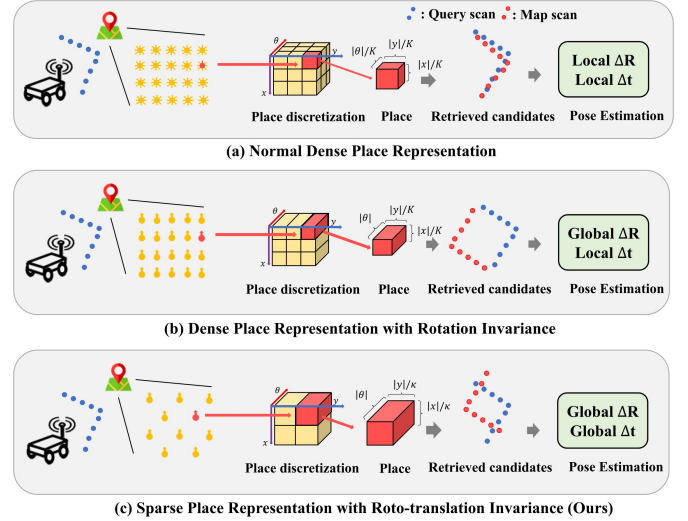


Fig. 1: Demonstration of global localization pipelines consisting of place recognition and pose estimation. $|\cdot|$ means the range of the axis. K and κ are the number of discretized bins and $K \gg \kappa$, which determines the density of place i.e. reference scans in the map. Our method aims at leveraging a sparse scan map for localization under large viewpoint differences using roto-translation invariant representation, as well as global convergent solvers.

discretized into many places. Accordingly, place recognition aims at finding the place to which the robot is closest. At the fine level, the search space is the continuous pose space centered at the pose of the place. Taking the pose of the place as initialization, the pose estimation process aims to obtain the accurate pose of the query. When the viewpoint difference is large, a query and a map scan taken in the same place can be different, which brings ambiguity to place recognition and calls for a large convergence basin in pose estimation.

To address the viewpoint difference, early works utilize 3-DoF (1-DoF rotation and 2-DoF translation) discretization [7]–[10], regarding scans with slight viewpoint differences as different places. This is illustrated in the first row of Fig. 1. Such formulation relaxes the place recognition to only considering small viewpoint difference, and simplifies the pose estimation to be local convergent, demonstrating good performance. But it calls for large memory to save dense places. The second row of Fig. 1 illustrates a pioneering work, Scan Context [3], [11], which regards scans with arbitrary rotation as the same place by explicitly modeling the rotation invariance for place representation. Besides, it proposes a global convergent rotation solver in the pose estimation stage,

*These two authors contribute equally to this work.

Code will be available at https://github.com/MaverickPeter/MR_SLAM

The authors are with Zhejiang University, Zhejiang, China. *Corresponding author: Yue Wang.* (e-mail: xuechengxu@zju.edu.cn; lusha@zju.edu.cn; wujun_csecyber@zju.edu.cn; luhaojian@zju.edu.cn; qgzhu@ipc.zju.edu.cn; lyyecho1119@gmail.com; rxiong@zju.edu.cn; wangyue@ipc.zju.edu.cn)

as no rotation initialization is available from place recognition with rotation invariance. Thus the discretization is reduced to 2-DoF (2D translation). Unfortunately, the rotation invariance is sensitive to the translation difference, hence requiring dense discretization in translation space. Considering the advantage of explicitly modeling rotation invariance, we raise a question: *Is it possible to build a representation that is invariant to both rotation and translation?*

In this paper, we address the large viewpoint difference in global localization using a sparse scan map. As illustrated in the third row in Fig. 1, we propose a framework RING++ that achieves *roto-translation invariance* for place recognition, and *global convergence* for both rotation and translation estimation, theoretically guaranteeing the performance under large viewpoint differences. Therefore, only a sparse discretization of map pose space in 2-DoF translation is sufficient. RING++ takes bird-eye view (BEV) of the scan, and processes in two passes: the representation pass for building roto-translation invariant representation and the solving pass for place recognition and pose estimation. In the representation pass, we exploit the properties of Radon transform and Fourier transform on BEV representation to generate roto-translation invariant place representation, and derive sufficient conditions of the feature extractor for the representation to preserve the roto-translation invariance. In the solving pass, the roto-translation invariant representation leads the successful place recognition even when large viewpoint differences exist between the query and map scans. By employing the cross correlation, the rotation and translation are further estimated with global convergence. To the best of our knowledge, RING++ is the first learning-free framework to address all subtasks of global localization in the sparse scan map. The experimental results validate our method in both place recognition and pose estimation, and show a superior performance compared to existing methods. To summarize, this work presents the following contributions:

- We propose a novel learning-free framework named RING++ for global localization on the sparse scan map, which can simultaneously solve place recognition and pose estimation tasks.
- We theoretically prove the roto-translation invariance property of our place representation. Meanwhile, the pose estimation solvers are presented with global convergence.
- We further derive sufficient conditions of feature extractors for the representation preserving the roto-translation invariance, enabling the framework to aggregate multi-channel features.
- We validate RING++ on three real-world datasets and multi-robot SLAM applications in the wild. We make the code, SLAM system, and evaluation tools all publicly available.

In the preliminary conference paper [12], we proposed a method that utilizes a single-channel occupancy map to generate roto-translation invariant place representation. In this paper, we formally state and prove the roto-translation invariance of our representation to provide a theoretical guarantee. Then we introduce the aggregation method to take multi-channel features into the framework, yielding better discrimination to

enhance both place recognition and pose estimation. We also derive the sufficient conditions of the feature extractor that can preserve the roto-translation invariance of our representation. Besides, we develop a global and effective correlation-based translation solver to address the outlier sensitivity in the conference version, which is non-trivial as the scans with large viewpoint differences must have less overlap. With all efforts above, the overall success rate of RING++ increases by almost 20%. We also validate the performance of RING++ with more ablation studies, substantial experiments with both learning-free and learning methods in diverse scenarios, as well as multi-robot collaborative SLAM.

II. RELATED WORKS

In this section, we provide a literature review on LiDAR-based recognition and estimation tasks with two main lines embedded in previous works. To begin with, local point features are evolving to represent the point cloud in a compact and efficient manner. To overcome noise and variances, different aggregation strategies are proposed to generate robust global representations with invariance properties from local features.

A. Feature Extraction

In the early stages of scan-based recognition, researchers focus on how to generate compact representations of scans. There are many ways to achieve this goal, but the early consensus is to find compact and effective local features. Geometric relations are first explored in many approaches. Stein et al. [13] propose Structural Indexing (SI) which constructs a representation from 3D curves and splashes. Rusu et al. [14] build PFH (Point Feature Histograms) by aggregating four handcrafted features which stem from normals and the distance between k-nearest point pairs. In the large-scale scene interpretation task, Weinmann et al. [15] provide eight semantic point features calculated by normalized eigenvalues of each point with its neighbors. With the wide use of local features, researchers found that fine resolution features are easily influenced by noises. To overcome this limitation, some coarser features are presented. Spin Image [16] counts point numbers in each volume of cylinder support around a keypoint. ESF [17] method uses voxel grids to approximate the surface and encodes shape properties. SHOT [18], [19] combines signature and histogram in a local reference frame and encodes the cosine value of the angle between the normal and the local z-axis at the feature point.

Although these features are widely used for scan-based recognition tasks, they are unstable when applied to the LiDAR-based place recognition scenario. The poor generalization performance is caused by the sensor characteristics of the newly equipped LiDAR. Points collected by LiDAR are unstructured and the sparsity of points varies along with the sensor range. In order to tackle this problem, learning-based methods are proposed. Due to the strong descriptive ability of the 2D convolution neural network (CNN), some researchers extend it to 3D cases by representing point clouds in 3D volumes [20]–[22]. However, these CNN-based methods usually introduce quantization errors and high computational

costs. To alleviate the drawbacks brought by CNN, PointNet [23] first learns features directly from the raw 3D point cloud data. PointNet++ [24] further introduces the hierarchical feature learning to learn local features with increasing scales. To better acquire relationships between local points, graph-based [10], [25] and kernel-based [26] networks are proposed. Other than geometry information, OverlapNet [27] and SSC [28] also take semantic clues into account. Some recent works propose fusion frameworks for incorporating image features as well [29]–[31]. Despite the fact that different methods provide different local features, they are all presented in a multi-channel manner. With this characteristic in mind, we propose a multi-channel framework that can be viewed as a feature aggregation module, allowing us to use different local features and improve discrimination with roto-translation invariance.

B. Aggregation and Invariance

With local features extracted, global descriptors are often generated by aggregating the local features. Early aggregation methods can be divided into two classes: signature and histogram.

Signature describes the 3D support by defining a local reference frame and encoding local features into the subset of the support. Histogram describes the support by encoding counts of local features. Structural Indexing [13] is one of the first methods to use signatures to capture 3D curves. 3D SURF [32] extends the mature 2D SURF [33] by voxelizing the 3D data and utilizing Haar wavelet response to determine the saliency of each voxel.

More previous works prefer the histogram since it provides a coarser representation of the point cloud that is robust to slight variance. PFH [14], [34] and VFH [35] are the early methods that explicitly introduce translation and rotation invariance. VFH finds the viewpoint directions and counts the angles between the normals in a histogram. SHOT [18] collects the histogram of normal angles in a spherical bin around a keypoint to build the descriptor. Rohling [7] first utilize histogram-based similarity measures in robotics systems to find loop closures.

With the appearance of learning-based local features, new aggregation methods are proposed in the place recognition task. NetVLAD [36], first introduced in visual place recognition, modifies VLAD [37] with learnable weights and integrates it into a CNN. Following the idea of NetVLAD, several methods [9], [10] apply NetVLAD to supervise the feature learning. DiSCO [38] utilizes Fourier transform to generate a global descriptor in the frequency domain. Apart from these specially designed aggregation methods, MinkLoc3D and its extensions [6], [39], [40] adopt the GeM [41] pooling layer to generate discriminative global descriptors.

Inspired by early works on rotation invariance, many approaches also focus on achieving invariance against viewpoint difference. M2DP [8] presents a multi-view projection on the point cloud and uses PCA to compensate viewpoint difference. LocNet [42] aggregates the distance of consecutive points in the same ring to a rotation invariant histogram and adopts a siamese network for feature learning. Iris [4] explicitly models rotation invariance using Fourier transform on polar images.

Previous works only present rotation invariant representation for place recognition, Scan context and its extension [3], [11] also realize lateral invariance and simultaneously estimate 1-DoF rotation and 1-DoF lateral translation, which is effective in autonomous driving. However, in Scan context, translation invariance is achieved through augmentation based on urban road assumptions. When there is a large difference in viewpoint, translation invariance is invalid. DiSCO [38] adopts the invariance property of the Fourier transform to simultaneously estimate rotation and achieve invariance. Since the polar transform used in DiSCO is not translation invariant, it suffers from the distortion caused by large translation variance. To overcome the influence brought by the large translation, Ding et al. [43] utilized Radon transform to estimate 1-DoF rotation with robust translation invariance. In this work, we further derive a multi-channel framework based on the Radon transform which can estimate the 3-DoF pose and preserve roto-translation invariance.

III. OVERVIEW

LiDAR-based global localization aims to estimate the pose T_Q of the query scan P_Q in a scan map $\mathfrak{M} \triangleq \{P_i, T_i\}$, which is a database populated by map scans P_i with registered poses T_i . In general, global localization is solved in two stages: place recognition and pose estimation. In the place recognition stage, a map scan with a large overlap with the query scan is retrieved from the map, denoted as P_n , which indicates that P_Q is collected at the place near P_n in the map. Then in pose estimation stage, the metric pose T_Q is achieved by estimating the relative pose T_{nQ} between P_Q and P_n , and applying T_{nQ} to T_n .

When the robot trajectory in the current session is different from the map session, P_Q and P_n can overlap but with T_Q and T_n being different, especially in rotation e.g. opposite direction. At the same time, $|\mathfrak{M}|$, the place density of a map, is expected to be sparse for storage and efficiency. As a result, the main challenge for place recognition is to build representation that is similar under large viewpoint differences, i.e. variance of the relative pose T_{nQ} , which further causes the challenge in pose estimation: the estimator should be globally convergent, as no reliable initial value for T_{nQ} is available.

A. Equivariance and Invariance

To deal with the pose variance in place recognition, the invariant representation of the scan is built. However, when the representation is invariant to relative pose, the pose estimation becomes impossible to solve, calling for additional representations bridging the raw scan and the invariant representation. Following this idea, we formally introduce equivariance and invariance in the context of global localization. The representation is denoted as an operation g taking the scan P as input. P_d and P_α indicate that the scan is translated by d , or rotated by α . g_d and g_α indicate that the representation is translated by d or rotated by α . Then we have the definitions:

Definition 1 (Translation Equivariance). *If the operation g is translation equivariant, it satisfies*

$$g_d(P) = g(P_d) \quad (1)$$

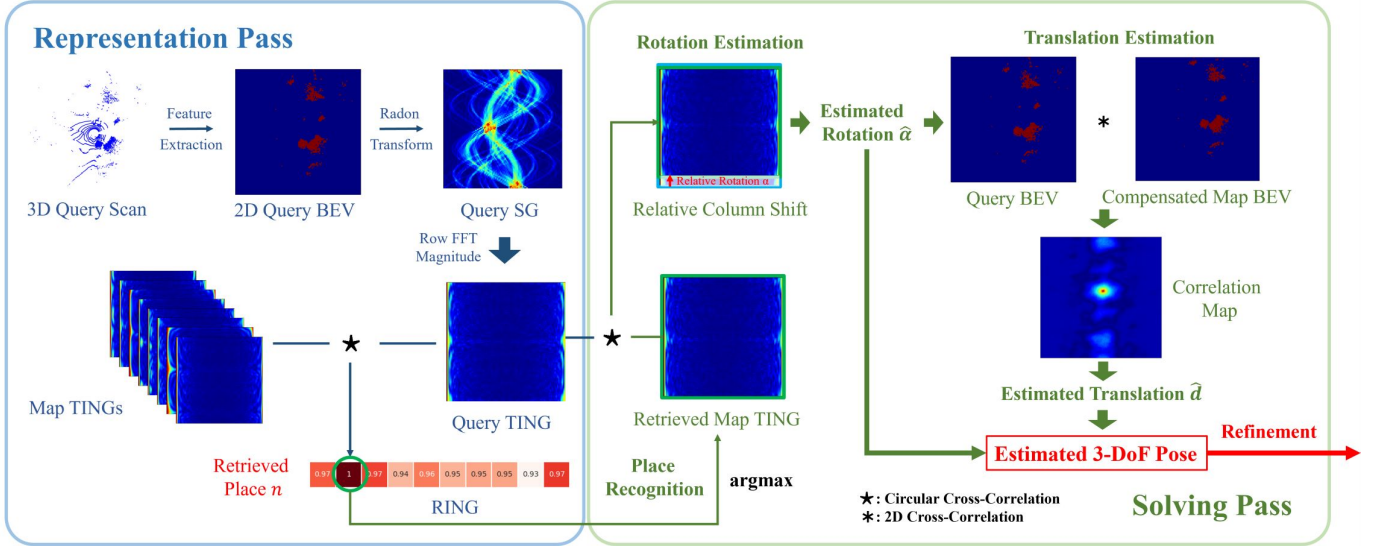


Fig. 2: Overall framework of the proposed method. RING representation is used for place recognition, TING representation is utilized for rotation estimation and BEV representation is leveraged for translation estimation.

Definition 2 (Rotation Equivariance). If the operation g is rotation equivariant, it satisfies the equation

$$g_\alpha(P) = g(P_\alpha) \quad (2)$$

Definition 3 (Translation Invariance). If the operation g is translation invariant, it satisfies the equation

$$g(P) = g(P_d) \quad (3)$$

Definition 4 (Rotation Invariance). If the operation g is rotation invariant, it satisfies the equation

$$g(P) = g(P_\alpha) \quad (4)$$

B. Framework

As shown in Fig. 2, RING++ extracts features from scans, and builds representations for place recognition, rotation estimation and translation estimation respectively. Totally, there are two passes in RING++, a forward representation pass and a backward solving pass.

In the representation pass, the rotation equivariant scan feature of P_Q is represented as sinogram (SG) by Radon transform (RT), then represented as translation invariant rotation equivariant gram (TING) by discrete Fourier transform (DFT), and finally represented as roto-translation invariant gram (RING) by batch circular cross-correlation.

In the solving pass, RING is utilized for place recognition with different query/mapping trajectories and low place density, by which the caused pose difference becomes invariant in RING. Then TING is utilized for relative rotation estimation given the retrieved map scan P_n , since the translation in TING is invariant. Finally, BEV is utilized for relative translation estimation after the rotation in BEV is compensated by the estimation. Thanks to the decoupling leveraged by invariance, rotation and translation in T_{nQ} can be solved independently via globally convergent solvers.

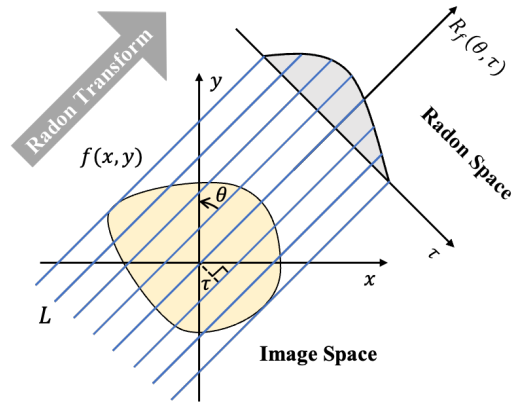


Fig. 3: Graph illustration of Radon transform, which demonstrates a single row of the sinogram with a constant θ after Radon transform.

IV. REPRESENTATION AND SOLVING

A. Representation Pass

1) *BEV*: The first step of RING++ is to extract the features from the scan. Following common pipelines, we eliminate the ground from the 3D point cloud. Then we voxelize the scan into a 3D volume, in which each voxel encodes the occupancy, indicating whether there is a point inside. With the extracted features, we accumulate the height dimension of 3D volume to generate a 2D BEV representation $f(x, y) \in \mathbb{R}$.

2) *Sinogram*: Given $f(x, y)$, we apply Radon transform \mathcal{R} to yield a sinogram. Radon transform is a linear integral transform which maps $f(x, y)$ from the original image space (x, y) to the Radon parameter space (θ, τ) , which is demonstrated in Fig. 3. Denoting the line for integral in Radon transform as L , we have

$$L : x \cos \theta + y \sin \theta = \tau \quad (5)$$

where $\theta \in [0, 2\pi)$ represents the angle between L and the y axis, and $\tau \in (-\infty, \infty)$ represents the perpendicular distance

from the origin to L . By formalizing the integral results into a 2D function with the Radon parameter as axes, we have $\mathcal{R}_f(L) = \mathcal{R}_f(\theta, \tau)$, namely sinogram (SG). Specifically, the Radon transform is calculated as:

$$\begin{aligned} \mathcal{R}_f(\theta, \tau) &= \int_{x \cos \theta + y \sin \theta = \tau} f(x, y) dx dy \\ &= \int_{-\infty}^{\infty} \int_{-\infty}^{\infty} f(x, y) \delta(\tau - x \cos \theta - y \sin \theta) dx dy \end{aligned} \quad (6)$$

where $\delta(\cdot)$ is the Dirac delta function.

When the robot revisits the same place with different rotation α and translation $d \triangleq (\Delta x, \Delta y)^T$, SG can reflect such relative pose as follows:

Rotation: A rotation of $f(x, y)$ by a rotation angle α results in a circular shift along θ axis of SG :

$$\mathcal{R}_f(\theta, \tau) \xrightarrow{\alpha} \mathcal{R}_f(\theta + \alpha, \tau) \quad (7)$$

A rotation leads to a uniform shift along θ axis of SG , which satisfies Definition 2 of rotation equivariance, arriving at the following result:

Lemma 1. SG is rotation equivariant.

Translation: A translation of $f(x, y)$ by d results in an angle-dependent shift of τ parameter on SG :

$$\mathcal{R}_f(\theta, \tau) \xrightarrow{d} \mathcal{R}_f(\theta, \tau - (\cos \theta, \sin \theta)d) \quad (8)$$

Different from the rotation, translation leads to a non-uniform shift along τ axis of SG .

Pose: With both rotation α and translation d , SG can be described by combining Eq. 7 and Eq. 8:

$$\mathcal{R}_f(\theta, \tau) \xrightarrow{\alpha, d} \mathcal{R}_f(\theta + \alpha, \tau - (\cos(\theta + \alpha), \sin(\theta + \alpha))d) \quad (9)$$

3) *TING*: To further eliminate the coupled effect of translation on the τ axis of SG in Eq. 8, we apply row-wise 1D DFT to SG along τ axis, and then calculate the magnitude of the resultant frequency spectrum. We name this representation as *TING*, denoted as $M_f(\theta, \omega)$, where ω is the sampled frequency in discrete the frequency spectrum.

Lemma 2. *TING* is rotation equivariant and translation invariant.

Proof of Lemma 2. Suppose $M'_f(\theta, \omega)$ is the *TING* representation constructed from transformed BEV $f'(x, y)$ by random translation d . Referring to the shift property of Fourier transform, we have:

$$\begin{aligned} M'_f(\theta_j, \omega) &= |\mathcal{F}(R_f(\theta_j, \tau - (\cos \theta_j, \sin \theta_j)d))| \\ &= |\mathcal{F}(R_f(\theta_j, \tau))e^{-i2\pi\omega(\cos \theta_j, \sin \theta_j)d}| \\ &= |\mathcal{F}(R_f(\theta_j, \tau))|e^{-i2\pi\omega(\cos \theta_j, \sin \theta_j)d}| \\ &= |\mathcal{F}(R_f(\theta_j, \tau))| \\ &= M_f(\theta_j, \omega) \end{aligned} \quad (10)$$

where $|\cdot|$ is the operation of taking magnitude, $\mathcal{F}(\cdot)$ is the DFT operator, and θ_j means a row in SG and the same row in *TING*. Therefore, *TING* satisfies Definition 3 of translation invariance.

As we only apply DFT to τ axis of SG , θ axis of *TING* keeps the same as that of SG , thus the rotation equivariance is reserved according to Lemma 1. \square

4) *RING*: The final step of the representation pass is to eliminate the effect of rotation. According to Eq. 7, note that the rotation only leads to the cyclic shift of θ axis of *TING*, we build the rotation-invariant representation in two steps. First, we employ a batch circular cross-correlation between *TING* M_Q of query scan P_Q and *TING* M_i of every map scan P_i in \mathfrak{M} , resulting in a batch of correlation maps as:

$$\begin{aligned} \mathfrak{C}_i(k_\theta, k_\omega) &= M_Q(\theta, \omega) * M_i(\theta, \omega) \\ &= \sum_{\theta_j} \sum_{\omega_m} M_Q(\theta_j + k_\theta, \omega_m + k_\omega) M_i(\theta_j, \omega_m) \end{aligned} \quad (11)$$

where $\mathfrak{C}_i(k_\theta, k_\omega)$ is the resultant 2D correlation map, k_θ and k_ω are the axes of the correlation map, and $*$ is the 2D cross-correlation operation between two images.

Since *TING* is translation invariant by Lemma 2, ω axis does not make any difference in 2D cross correlation calculation. Therefore, 2D cross correlation between two *TING*s can be reduced to 1D cross correlation along θ axis, which is derived by substituting $k_\omega = 0$ into Eq. 11:

$$\begin{aligned} \mathfrak{C}_i(k_\theta) &= M_Q(\theta, \omega) \star M_i(\theta, \omega) \\ &= \sum_{\theta_j} \sum_{\omega_m} M_Q(\theta_j + k_\theta, \omega_m) M_i(\theta_j, \omega_m) \\ &= \sum_{\theta_j} M_Q(\theta_j + k_\theta) M_i(\theta_j)^T \end{aligned} \quad (12)$$

where $\mathfrak{C}_i(k_\theta)$ is the resultant 1D correlation map, k_θ is the axis of $\mathfrak{C}_i(k_\theta)$, and \star is the 1D circular cross-correlation that we derive from 2D one. Then, we take the max pooling on the correlation map \mathfrak{C}_i of each *TING* pair (M_Q, M_i) , comprising the final vector representation named *RING* $N_Q \in \mathbb{R}^{|\mathfrak{M}|}$:

$$N_{Q,i} = \max_{k_\theta} \mathfrak{C}_i(k_\theta) \quad (13)$$

where $N_{Q,i}$ is the i th element of N_Q . Then we arrive at the first theorem:

Theorem 1. *RING* is roto-translation invariant.

Proof of Theorem 1. Applying the rotation α and translation d to P_Q , we denote the resultant SG as R'_Q as Eq. 9:

$$R'_Q(\theta, \tau) = R_Q(\theta + \alpha, \tau - (\cos(\theta + \alpha), \sin(\theta + \alpha))d) \quad (14)$$

Based on Lemma 2, the *TING* M'_Q of transformed SG R'_Q is:

$$\begin{aligned} M'_Q(\theta_j, \omega) &= |\mathcal{F}(R'_Q(\theta_j, \tau))| \\ &= |\mathcal{F}(R_Q(\theta_j + \alpha, \tau - (\cos(\theta_j + \alpha), \sin(\theta_j + \alpha))d))| \\ &= M_Q(\theta_j + \alpha, \omega) \end{aligned} \quad (15)$$

The correlation map between M'_Q and M_i is formulated as:

$$\begin{aligned} \mathfrak{C}'_i(k_\theta) &= M'_Q(\theta, \omega) \star M_i(\theta, \omega) \\ &= M_Q(\theta + \alpha, \omega) \star M_i(\theta, \omega) \\ &= \mathfrak{C}_i(k_\theta + \alpha) \end{aligned} \quad (16)$$

Based on Eq. 16, the invariance of max value with respect to shift leads to the equality between RING N_Q and RING N'_Q derived as:

$$N_{Q,i} = \max_{k_\theta} \mathfrak{C}_i(k_\theta) = \max_{k_\theta} \mathfrak{C}_i(k_\theta + \alpha) = N'_{Q,i} \quad (17)$$

Thus RING is roto-translation invariant. \square

Now we summarize the representations in forward representation pass in brief: the rotation equivariant SG, the rotation equivariant and translation invariant TING, and the roto-translation invariant RING. RING of a scan stays the same even if large viewpoint changes are present.

B. Solving Pass

1) *Place Recognition*: Put Theorem 1 in a real scenario. Due to the finite scan range occlusion, the invariance of RING cannot be guaranteed when translation is significant with respect to the scan range occlusion. Therefore, we have RING that is invariant given an arbitrary rotation change, but gradually degenerated with respect to larger translation changes. Following this result, we can set the range of a place by measuring the change of RING. On the other hand, the density of the place for successful global localization is able to reflect the robustness against the difference between the trajectory in the query and mapping session.

Based on the difference between RINGs of query and map scans, we can retrieve the minimum one as the place n where the query scan lies, arriving at place recognition:

$$n = \arg \min_i \|N_Q - N_i\| \quad (18)$$

However, the dimension of RING is $|\mathfrak{M}|$, which is computed and stored for all $|\mathfrak{M}|$ map scans, resulting in total storage and nearest neighbor search of $O(|\mathfrak{M}|^2)$, which may not be affordable for onboard processing.

To reduce the computation, we introduce an approximation to Eq. 18 by checking the maximum element in N_Q :

$$n = \arg \max_i \tilde{N}_{Q,i} \quad (19)$$

where \tilde{N} is the normalized RING calculated from normalized TING \tilde{M} with zero mean and unit variance. The aim of normalization is to eliminate the effect from the finite scan range e.g. number of valid scan points. In this way, we avoid the computation and storage of RINGs for all map scans. The equivalence between Eq. 18 to Eq. 19 is shown in Appendix A. We show that the prerequisite for Eq. 19 is practical in real applications and hence is employed in the experiments.

2) *Pose Estimation*: After place recognition, we estimate the relative pose T_{nQ} between P_Q and P_n . Denote f_n and M_n as the BEV and TING of the retrieved map scan P_n respectively. Given the local planar ground surface [44], the relative pitch, roll and height between query and map pose should be small. Therefore, we first estimate a reduced 3-DoF relative pose globally without initial value, comprising 1-DoF rotation α and 2-DoF planar translation d , then estimate the 6-DoF relative pose with the resultant 3-DoF relative pose as an initial value. To address the first step, we leverage TING

to estimate rotation α , which is then utilized to compensate BEV for estimation of translation d . For the second step, with the pose above as the initial value, we refine the metric pose using ICP [45].

Rotation Estimation: Rotation estimation is achieved based on the TING. In Eq. 13, the maximum value occurs when M_Q is equal to M_n . Given correct place recognition, as TING is translation invariant according to Lemma 2, M_Q and M_n should be related by a relative rotation, and the equality is achieved when the shift k_θ equals to the real relative rotation.

Therefore, we regard the shift achieving the maximum value along θ axis as the estimation of relative rotation between P_Q and P_n , denoted as $\hat{\alpha}$

$$\hat{\alpha} = \arg \max_{k_\theta} \tilde{\mathfrak{C}}_n(k_\theta) \quad (20)$$

where $\tilde{\mathfrak{C}}$ is the normalized correlation map calculated from the normalized TING \tilde{M} . The normalization is employed to relieve the effect of finite scan range and discretization in practice. It is important that the estimator be global convergent without dependency on any initial values. It is actually an exhaustive search, thus keeping the optimality. With the aid of fast Fourier transform (FFT) and parallel computing, this exhaustive process is fast. Refer to Appendix B for derivation.

Translation Estimation: Based on the rotation estimation, we can rotate the BEV $f(x, y)$ by $-\hat{\alpha}$ to eliminate the relative rotation between $f_Q(x, y)$ and $f_n(x, y)$, yielding a compensated BEV $f'_n(x, y)$. With the rotation variance eliminated, 2D cross correlation can be applied to solve the translation.

$$\mathfrak{C}_n(k_x, k_y) = f_Q(x, y) * f'_n(x, y) \quad (21)$$

where $\mathfrak{C}(k_x, k_y)$ is the correlation map of two BEVs. k_x and k_y are the axes of the correlation map. As for rotation, the maximum correlation in Eq. 21 should peak at the real relative translation. Denoting the estimated translation in correlation map as \hat{d} , we have

$$\hat{d} = \arg \max_{k_x, k_y} \mathfrak{C}_n(k_x, k_y) \quad (22)$$

Benefiting from the cross correlation, the translation estimation is globally convergent.

Refinement: With the rotation $\hat{\alpha}$ and translation \hat{d} estimated above, an initial value is built by setting the relative pitch, roll and height with zeros. Theoretically, the estimation accuracy is up to the resolution of the BEV and Radon transform, thus keeping the convergence of the local refinement algorithm with high probability. In this paper, ICP is employed for refinement. Finally, we arrive at the 6-DoF pose \hat{T}_{nQ} , which is further applied to T_n as the query pose estimation \hat{T}_Q .

C. Perspective of Feature Aggregation

A typical pipeline [37] for representation in place recognition consists of feature extraction and feature aggregation. In feature extraction, local features of sparse keypoints [33]–[35], [46], or dense points [10] are extracted, which is fed to the feature aggregation module to build a global feature for

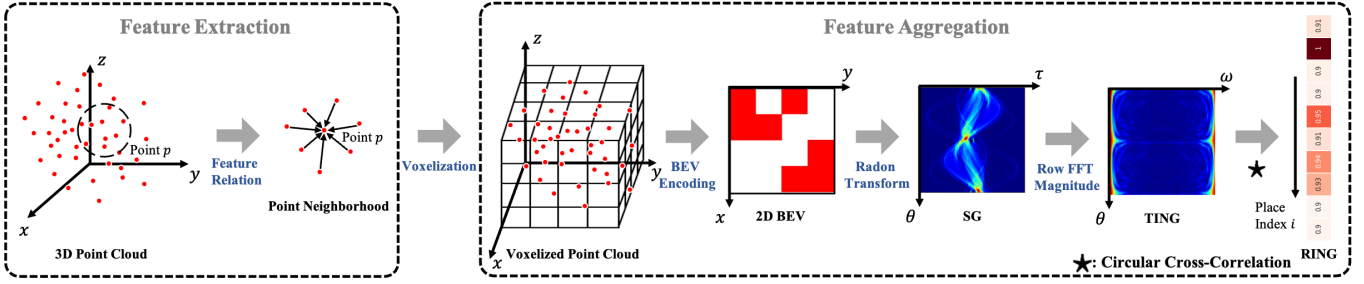


Fig. 4: Pipeline of the single-channel framework of our method, including feature extraction and feature aggregation.

the scan, say global max pooling, generalized-mean pooling (GeM) [41], or VLAD [37], [47] etc.

Our method also fits the pipeline, as illustrated in Fig. 4. The feature extraction is achieved by occupancy BEV representation from raw scan. The feature aggregation is achieved by the representation pass. The advantage of the proposed feature aggregation is the representation property, which is roto-translation invariant for place recognition, and equivariant for pose estimation. As a general feature aggregation $g(\cdot)$, the feature extraction part can be switched to others, which is discussed in the next section.

V. MULTI-CHANNEL FRAMEWORK

An intuitive improvement is to replace the simple binary BEV feature with one that takes more structured information in the height dimension. Naturally, we investigate the question: what are the requirements for feature extraction that is able to preserve the equivariance/invariance of SG, TING and RING?

A. Feature Extraction

We begin with the second theorem to present sufficient conditions for feature extraction:

Theorem 2. *Let $E(\cdot)$ be an feature extractor, $g(\cdot)$ be a roto-translation invariant feature aggregation. Then the representation produced by $g(E(\cdot))$ preserves both translation and rotation invariance if one of the following requirements is satisfied:*

- $E(\cdot)$ is equivariant to both translation and rotation.
- $E(\cdot)$ is invariant to both translation and rotation.

Proof of Theorem 2. Let P be a point cloud as the initial input of $E(\cdot)$. Utilizing the feature aggregation method $g(\cdot)$ to the features exploited by the feature extractor $E(\cdot)$, we can obtain the aggregated result $g(E(P))$. Since $g(\cdot)$ is invariant to both translation and rotation, $g(E(P)) = g(E_d(P))$ by Definition 3 and $g(E(P)) = g(E_\alpha(P))$ by Definition 4. Theorem 2 includes totally two cases, so we divide the proof into two sub-proofs corresponding to the two cases.

Case 1: If $E(\cdot)$ is equivariant to both translation and rotation, then $E_d(P) = E(P_d)$ by Definition 1 and $E_\alpha(P) = E(P_\alpha)$ by Definition 2.

Combining $E_d(P) = E(P_d)$ and $g(E(P)) = g(E_d(P))$, we have:

$$g(E(P)) = g(E_d(P)) = g(E(P_d)) \quad (23)$$

TABLE I: Extracted Features of RING++

Feature	Formulation
Change of curvature	$\frac{\lambda_3}{\sum_{j=1}^3 \lambda_j}$
Omni-variance	$\frac{\sqrt[3]{\prod_{j=1}^3 \lambda_j}}{\sum_{j=1}^3 \lambda_j}$
Eigenvalue-entropy	$-\sum_{j=1}^3 (\lambda_j \ln \lambda_j)$
2D linearity	$\frac{\lambda_{2D,2}}{\lambda_{2D,1}}$
Maximum height difference	$Z_{max} - Z_{min}$
Height variance	$\sum_{k=1}^{30} \left(\frac{Z_k - \sum_{k=1}^{30} Z_k}{30} \right)^2$

* $\lambda_1 \geq \lambda_2 \geq \lambda_3 \geq 0$ represent the ordered eigenvalues of the symmetric positive-definite covariance matrix of the neighborhood.

Combining $E_\alpha(P) = E(P_\alpha)$ and $g(E(P)) = g(E_\alpha(P))$, we have:

$$g(E(P)) = g(E_\alpha(P)) = g(E(P_\alpha)) \quad (24)$$

From Definition 3 and 4, we can conclude that the the final representation $g(E(P))$ is translation invariant and rotation invariant.

Case 2: If $E(\cdot)$ is invariant to both translation and rotation, then $E(P) = E(P_d)$ by Definition 3 and $E(P) = E(P_\alpha)$ by Definition 4.

Combining $E(P) = E(P_d)$ and $g(E(P)) = g(E_d(P))$, we have:

$$g(E_d(P)) = g(E(P)) = g(E(P_d)) \quad (25)$$

Combining $E(P) = E(P_\alpha)$ and $g(E(P)) = g(E_\alpha(P))$, we have:

$$g(E_\alpha(P)) = g(E(P)) = g(E(P_\alpha)) \quad (26)$$

From Definition 3 and 4, we can conclude that the the final representation $g(E(P))$ is translation invariant and rotation invariant. \square

As stated in Theorem 1, the proposed aggregation method $g(\cdot)$ possesses translation and rotation invariance, which satisfies the requirement of an aggregation method in Theorem 2. Thus, we build rotation invariant and translation equivariant features to preserve the property of the aggregation. We select six rotation invariant translation equivariant features from previous literature [15] shown in Tab. I. Note that popular features like Harris3D [46], SIFT3D [48], FPFH [34] and SHOT [18] can also fit in the framework, some of which are leveraged for ablation study in Section VII-D. Specifically, the local feature is built in two steps. First, for each point p in the scan, we

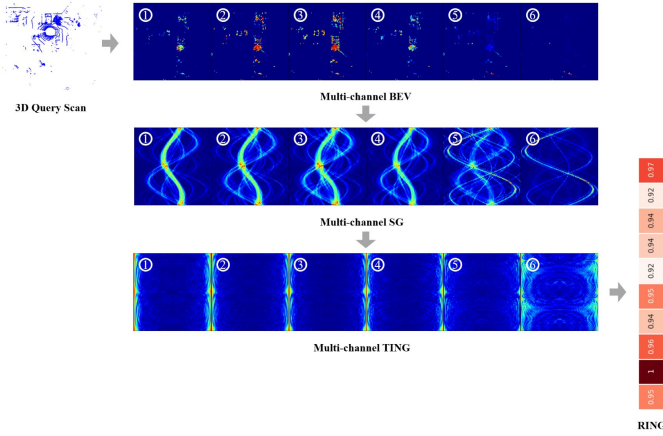


Fig. 5: Visualization of the multi-channel representation pass. With six extracted local features, the corresponding BEV, SG and TING are 6-channel.

extract features from its 30-neighborhood as shown in Tab. I. Then we accumulate the point features along the dimension of height. For all point features belonging to the same BEV grid, we use the channel-wise max pooling, resulting in a 6-channel BEV, $f(x, y) \in \mathbb{R}^6$. Denote each channel of $f(x, y)$ as $f_c(x, y) \in \mathbb{R}$, where $c \in \{1, 2, 3, 4, 5, 6\}$ indicates the channel dimension. Compared with the occupancy, this feature better encodes the information in the height dimension such as the building facade.

After feature extraction, we embark on feature aggregation, following the same pipeline demonstrated in Section IV to represent. One remaining problem is to aggregate the multi-channel feature into one for solving.

B. Multi-channel Representation Pass

For clear demonstration, we visualize the multi-channel representation pass in Fig. 5. Based on the 6-channel BEV $f(x, y)$, we apply Radon transform to each BEV channel $f_c(x, y)$, yielding a SG channel $R_{f_c}(\theta, \tau)$. By concatenating all $R_{f_c}(\theta, \tau)$ along channel dimension c , we can obtain a 6-channel SG $R_f(\theta, \tau)$.

After that, we employ row-wise DFT to $R_{f_c}(\theta, \tau)$ and take the magnitude spectrum of the result, denoted as $M_{f_c}(\theta, \omega)$, to achieve translation invariance. In the same manner, we concatenate all $M_{f_c}(\theta, \omega)$ along c dimension, yielding a 6-channel TING $M_f(\theta, \omega)$.

Next we implement 1D circular cross-correlation between query TING $M_Q(\theta, \omega)$ and all map TINGs $M_i(\theta, \omega)$. For each channel TING pair ($M_{Q_c}(\theta, \omega), M_{i_c}(\theta, \omega)$), we can get a 1D correlation map $\mathfrak{C}_{i_c}(k_\theta)$:

$$\begin{aligned} \mathfrak{C}_{i_c}(k_\theta) &= M_{Q_c}(\theta, \omega) \star M_{i_c}(\theta, \omega) \\ &= \sum_{\theta_j} M_{Q_c}(\theta_j + k_\theta) M_{i_c}(\theta_j)^T \end{aligned} \quad (27)$$

Then we sum all $\mathfrak{C}_{i_c}(k_\theta)$ along c dimension, generating a single-channel 1D correlation map $\mathfrak{C}_i(k_\theta)$:

$$\mathfrak{C}_i(k_\theta) = \sum_{c=1}^6 \mathfrak{C}_{i_c}(k_\theta) \quad (28)$$

Finally we take the maximum value of $\mathfrak{C}_i(k_\theta)$ as the i th element of the final representation RING N_Q , which is the same as Eq. 13.

C. Multi-channel Solving Pass

In the solving pass, we perform place recognition with rotation-invariant global descriptor RING N_Q first. Utilizing the same operation in Eq. 19, we retrieve the closest map scan P_n from \mathfrak{M} by finding the index of the maximum element in N_Q .

Then we carry out pose estimation including three steps: rotation estimation, translation estimation and refinement. Taking advantage of the summed correlation map $\mathfrak{C}_n(k_\theta)$ between the query TING M_Q and the retrieved map scan TING M_n , the relative rotation can be easily estimated by Eq. 20, which is the optimal shift when M_Q best aligns with M_n . To solve the relative translation d , we begin with compensating the BEV $f_Q(x, y)$ via rotating $f_n(x, y)$ by $-\hat{\alpha}$. Under the multi-channel framework, we first calculate the correlation map of each channel $\mathfrak{C}_{n_c}(k_x, k_y)$ using Eq. 21 and then sum the correlation maps along the channel dimension to obtain the globally optimal translation \hat{d} :

$$\hat{d} = \arg \max_{(k_x, k_y)} \sum_{c=1}^6 \mathfrak{C}_{n_c}(k_x, k_y) \quad (29)$$

The refinement for multi-channel framework is exactly the same as the single-channel one. The estimated 3-DoF relative transformation between P_Q and P_n is utilized as the initial value for ICP to acquire the refined 6-DoF pose \hat{T}_Q .

VI. DATASET AND EVALUATION CRITERIA

In this section, we describe the datasets and evaluation criteria that we employ for performance validation.

A. Dataset

We perform our RING++ method on three widely used datasets for place recognition evaluation: NCLT [49], MulRan [50], and Oxford [51] datasets. In order to validate the translation and rotation invariance of our approach, we select several trajectories with large translation and rotation changes. Furthermore, we utilize different sequences for multi-session place recognition evaluation. The characteristics of these sequences are detailed in the subsections.

1) *NCLT Dataset*: A large-scale and long-term dataset collected by a Segway robot on the University of Michigan's North Campus. It contains 27 different sessions that captured biweekly from January 8, 2012 to April 5, 2013. Covering the same trajectory over 15 months, the dataset includes a large variety of environmental changes: dynamic objects like moving people, seasonal changes like winter and summer, and structural changes like the construction of buildings.

2) *MulRan Dataset*: A multimodal range dataset containing Radar and LiDAR data specially collected in the urban environment. It covers four different target environments: DCC, KAIST, Riverside, and Sejong City, providing both temporal and structural diversity for place recognition research.

3) *Oxford Radar RobotCar Dataset*: An extension to the *Oxford RobotCar Dataset* [52] for autonomous driving research. The data comprises 32 traversals of a central Oxford route in January 2019. A variety of weather and lighting conditions are encompassed in this dataset. A pair of Velodyne HDL-32E 3D LiDARs are mounted on the left and right sides of the vehicle to improve 3D scene understanding performance. For the convenience of place recognition evaluation, we concatenate point clouds collected by these two LiDARs into one single scan.

B. Evaluation Metrics

1) *Recall@1*: We utilize *Recall@1* [53] metric to evaluate a place recognition system in terms of the number of true loop candidates. *Recall@1* is defined as the ratio of top 1 true positives to total positives, which is formulated as

$$Recall@1 = \frac{TP_{top1}}{TP_{top1} + FN_{top1}} \quad (30)$$

where TP_{top1} denotes the number of true positives with top 1 retrieval, FN_{top1} denotes the number of false negatives with top 1 retrieval.

2) *Precision-Recall Curve*: For place recognition task, *precision* [53] is defined as the ratio of true positives to total matches, and *recall* [53] is defined as the ratio of true positives to total positives. The mathematical expressions are

$$Precision = \frac{TP}{TP + FP} \quad (31)$$

$$Recall = \frac{TP}{TP + FN} \quad (32)$$

where TP denotes the number of true positives, FP denotes the number of false positives, and FN denotes the number of false negatives. *Precision-Recall Curve* [54] is plotted under various thresholds. A point in the *Precision-Recall Curve* depicts the *precision* and *recall* values corresponding to a specific threshold.

3) *F1 score-Recall Curve*: *F1 score* [55] is the harmonic mean of precision and recall, combining precision and recall metrics into a single metric:

$$F1\ score = \frac{2 \times Precision \times Recall}{Precision + Recall} \quad (33)$$

which is a suitable metric to balance *precision* and *recall*.

4) *TE and RE*: We calculate average translation error TE and rotation error RE following [40], [56] for pose estimation evaluation. Since our method only yields 3-DoF poses, we evaluate 2-DoF translation and 1-DoF rotation error in the majority of evaluations. The mathematical formulas are

$$TE = \|\hat{d} - d^*\| \quad (34)$$

$$RE = |\hat{\alpha} - \alpha^*| \quad (35)$$

where \hat{d} and $\hat{\alpha}$ are the estimated 2-DoF translation and 1-DoF rotation. d^* and α^* are the ground-truth translation and rotation. Pose error calculation of incorrectly matched scans (i.e. not from the same place) is meaningless. Thus, we only compute the estimated pose errors of successfully matched pairs to compare the pose estimation performance.

5) *Success Rate*: To quantitatively evaluate the overall global localization performance, we leverage *Success Rate* [40], [56] metric which takes *Recall@1*, TE and RE into account, with both place recognition and pose estimation involved. Following the definition of *Success Rate* in [40], [56], *Success Rate* is calculated by the percentage of successfully aligned matches whose TE is below $2m$ and RE is below 5° . The mathematical formula is

$$Success\ Rate = \frac{TP_{TE < 2m \ \& \ RE < 5^\circ}}{TP + FP} \quad (36)$$

where $TP_{TE < 2m \ \& \ RE < 5^\circ}$ denotes the number of true positives whose translation error is below $2m$ and rotation error is below 5° .

6) *ATE*: Absolute trajectory error (*ATE*) is used to evaluate the performance of SLAM systems. It directly measures the difference between points of the true and the estimated trajectory. The *ATE* of i_{th} frame is formulated as below

$$ATE_i = \|\mathit{trans}(Q_i^{-1}SP_i)\| \quad (37)$$

where Q_i is the ground truth pose and P_i is the estimated pose. $S \in SE(3)$ is the transformation matrix to align the two poses, which is calculated by the least square method. $\mathit{trans}(\cdot)$ represents the translation part of the pose difference. In this paper, we use the average *ATE* to evaluate the performance of SLAM systems.

C. Comparative Methods

In terms of place recognition and pose estimation, we compare our approach against state-of-the-art learning-free and learning-based methods:

- **M2DP** [8] projects the point cloud to multiple 2D planes and leverages the singular vector of all signatures for points in each plane as the global descriptor to detect loop closure.
- **Fast Histogram** [7] utilizes the histogram of range distance directed extracted from the 3D point cloud as the global descriptor of the point cloud for loop closure detection.
- **Scan Context** [3] encodes the 3D scan to a representation called Scan Context which contains 2.5D information, compared to histogram-based methods. It is invariant to rotation changes via a two-phase search algorithm.
- **Scan Context++** [11] introduces two sub-descriptors to combine topological place recognition with 1-DoF semi-metric localization, so as to enhance the performance of Scan Context.
- **PointNetVLAD** [9] combines PointNet and NetVLAD to extract the global descriptor for a 3D point cloud by end-to-end training.
- **DiSCO** [38] encodes a 3D scan to a scan context and then uses an encoder-decoder network to extract features. It constructs a rotation invariant place descriptor by taking the magnitude of the frequency spectrum for place recognition and designs a correlation-based rotation estimator for 1-DOF pose estimation.
- **EgoNN** [40] designs a fully convolutional architecture to extract global and local descriptors. It uses the global

descriptor for coarse place recognition and the local descriptors for 6-DoF pose estimation.

D. Our Methods

In Section IV and V, we solve place recognition problem utilizing RING representation constructed from TING and estimate the relative rotation based on TING. To validate the translation invariance of RING generated by TING, we directly construct RING representation based on SG representation skipping TING formation process for place recognition, and then estimate the relative rotation and translation based on SG, which serves as a variant of our method. Taking feature extraction into account, we then have four versions of our method: RING (SG), RING, RING++ (SG), and RING++. By comparing the four versions, we can figure out the effects of translation invariance design and feature extraction on place recognition and pose estimation results.

- **RING (SG)** encodes occupancy information of a point cloud to SG and RING representations. It utilizes RING representation for place recognition, SG representation for rotation estimation, and single-channel BEV representation for translation estimation.
- **RING** encodes occupancy information of a point cloud to SG, TING and RING representations. It leverages RING representation for place recognition, TING representation for rotation estimation, and single-channel BEV representation for translation estimation.
- **RING++ (SG)** extracts multiple local features of a point cloud, following a multi-channel framework. It utilizes RING representation for place recognition, SG representation for rotation estimation, and multi-channel BEV representation for translation estimation.
- **RING++** extracts multiple local features of a point cloud, following a multi-channel framework. It leverages RING representation for place recognition, TING representation for rotation estimation, and multi-channel BEV representation for translation estimation.

E. Implementation Details

For a fair comparison, we remove the ground plane of the raw point cloud and filter it to the same range $[-70m, 70m]$ for all methods. For both Scan Context and our method, we set the grid size of BEV to 120×120 , so the translation resolution is $140/120 = 1.17m/pixel$ and the rotation resolution is $360/120 = 3^\circ/pixel$. The number of candidates of Scan Context++ is 10. The parameters and settings of other compared methods are kept the same as those in the original papers.

PointNetVLAD and DiSCO are retrained on the MulRan dataset. The output dimension of these two methods is set to 1024. In training step, places within $10m$ are regarded as positive pairs, while negative pairs are at least $20m$ apart. Other parameter configurations are similar to those in the original paper. For EgoNN, we use the publicly available pre-trained model for better performance. The output global descriptor dimension of EgoNN is 256, while the local descriptor dimension is 128. We use ICP implementation from

Open3D [57] in the experiments with pose refinement. The parameters of ICP are set according to common practice: *max correspondence distance* is 1.5m and *iterations* is 100.

VII. EXPERIMENTAL EVALUATION

In this section, we design some experiments to verify that the proposed approach:

- has strong translation invariance and rotation invariance that is independent of translational difference.
- detects the loops successfully when the pose difference between query and map point clouds is large.
- estimates a 3-DoF pose as a qualified initial guess for further metric refinement (ICP alignment).
- is computation-efficient with a compact representation for real-time applications.
- is easily pluggable into SLAM systems for loop closure detection and relocalization.

A. Illustrative Toy case Study

We present two toy cases to validate the effectiveness of our approach in terms of global localization. Specifically, we design a toy case to verify the roto-translation invariance of our representation RING for place recognition. Moreover, we investigate the impact of translation motion on relative rotation estimation utilizing various representations (SC (Scan Context), SG and TING), in order to highlight the advantage of our representation for pose estimation.

1) *Place Recognition Illustration*: We begin with a toy case study to illustrate the feasibility of our method for place recognition. In this toy case, we perform place retrieval in a scan map with 10 map scans for simplification. To better illustrate the proposed method, we visualize all the intermediate representations, as shown in Fig. 6. The top block (a) of Fig. 6 shows that the query scan is located at the same place where the second map scan lies according to Eq. 19. The retrieved map scan, i.e., the second map scan follows the representation pass which is depicted in the bottom block (b) of Fig. 6. Furthermore, the Euclidean distance between query RING and positive map RING is the smallest, which satisfies Eq. 18, and is also consistent with the retrieved result above by Eq. 19.

2) *Pose Estimation Illustration*: Similar to Scan Context series [3], [11], we leverage rotation-equivariant representations SG and TING to estimate the relative rotation, referring to rotation equivariance illustrated in Lemma 1 and 2. To distinguish our representation from others, we rotate the point cloud within $[0^\circ, 360^\circ)$ and translate the point cloud within $[-5m, 5m]$. After that, we employ the three aforementioned representations to estimate the relative rotation between the original point cloud and the transformed point cloud. The resolution of all representations for rotation estimation is the same, $3^\circ/pixel$. As we can easily see in Fig. 7, SC representation is strongly affected by translation difference. When the relative translation is beyond $1m$, the rotation estimation error rises to about 30° . In contrast, our representations SG and TING are much more robust to translation perturbation, showing smaller rotation estimation error. In addition, TING equipped with translation invariance is almost not influenced by translation

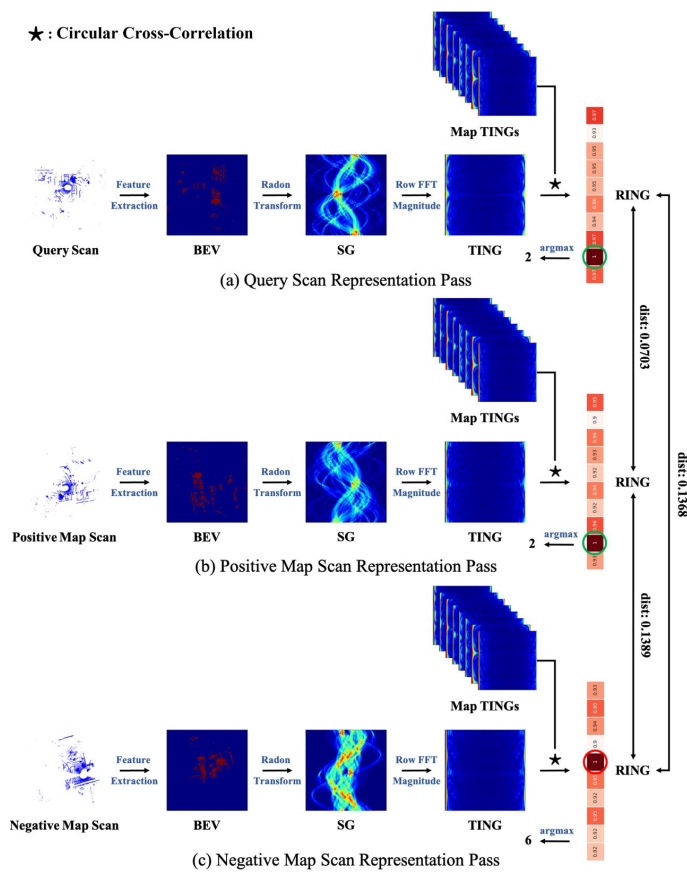


Fig. 6: Visualization of the representation pass for query scan, positive map scan and negative map scan, to verify the feasibility of utilizing Eq. 19 to equivalently replace Eq. 18 for place recognition. (a) The maximum value of RING representation points to the second scan in the scan map, which is the positive map scan shown in (b). (b) The RING representation of the positive map scan is the closest to the RING representation of query scan in terms of Euclidean distance. (c) The Euclidean distance between query RING and negative map RING is nearly twice of that between query RING and positive map RING.

disturbance, whose rotation estimation error keeps nearly 0° for all translation within $5m$.

B. Evaluation of Place Recognition

For comprehensive place recognition evaluation, we evaluate the proposed method regarding both online loop closure detection (single-session scenarios) and long-term localization (multi-session scenarios).

1) *Single-session Scenarios*: Under single-session scenarios, we select “2012-02-04” sequence in NCLT dataset, “DCC01” sequence in MulRan dataset, and “2019-01-11-13-24-51” sequence in Oxford dataset for place recognition evaluation. To verify the advantage of our approach in the sparse scan map, we perform all methods to detect loop closure online at different place density ($10m$, $20m$ and $50m$). *Precision-Recall Curve* and *F1 score-Recall Curve* are utilized as the evaluation metrics of single-session scenarios, as depicted in Fig. 8 and 9. As we can see, our RING-based methods are less

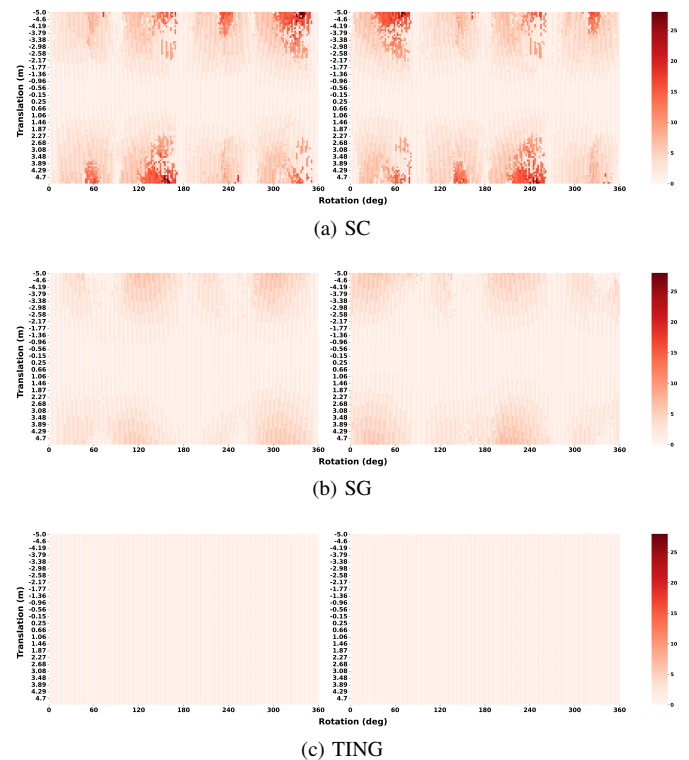


Fig. 7: Rotation estimation error using different representations. The left column shows the rotation estimation error with translation along the x-axis, and the right column shows the rotation estimation error with translation along the y-axis.

affected by place density than others. At $10m$ place density, RING-based methods show competitive performance with SC-based methods. However, with the decrease of place density, the translation between the query scan and the retrieved map scan enlarges, so our methods outperform them by an increasing margin. Compared with RING (SG) and RING++ (SG), RING and RING++ remain high-performance even at $50m$ place density, which validates the strong translation invariance of RING representation based on TING. The comparison result is consistent with the toy case result illustrated in Fig. 7, validating the robustness to translation of our methods and SC-based methods. Compared with RING (SG) and RING++ (SG) respectively, RING++ (SG) and RING++ achieve better performance, which is more obvious at lower place density. It demonstrates that the extracted local features are beneficial for place representation, thereby improving discrimination. In terms of Fast Histogram, the histogram aggregation is invariant to the rotation difference in the dense place representation. However, without the design of translation invariance, the performance on sparse place representation is limited. In terms of M2DP, the projection strategy improve discrimination but also cannot handle the scenario in which point cloud centerings are not well aligned.

2) *Multi-session Scenarios*: From the viewpoint of long-term autonomy, a robust place recognition system should work well when the surroundings change as time passes. To compare long-term place recognition performance, we select several inter-sessions covering the same region to serve as

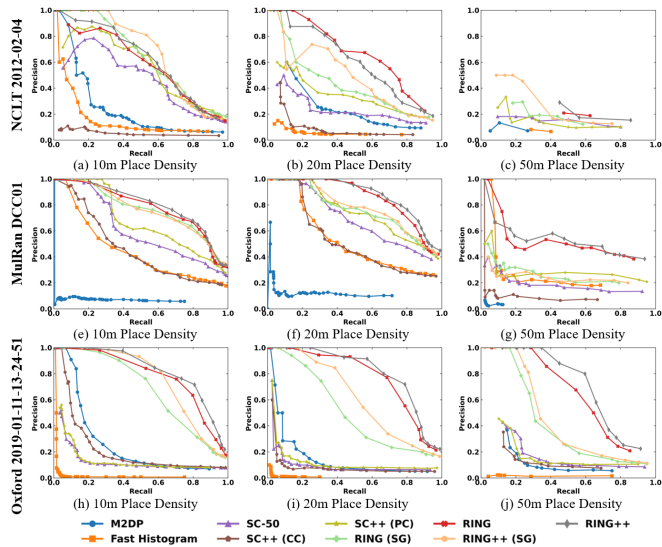


Fig. 8: Precision-Recall Curve for NCLT, MulRan and Oxford datasets under single-session scenarios.

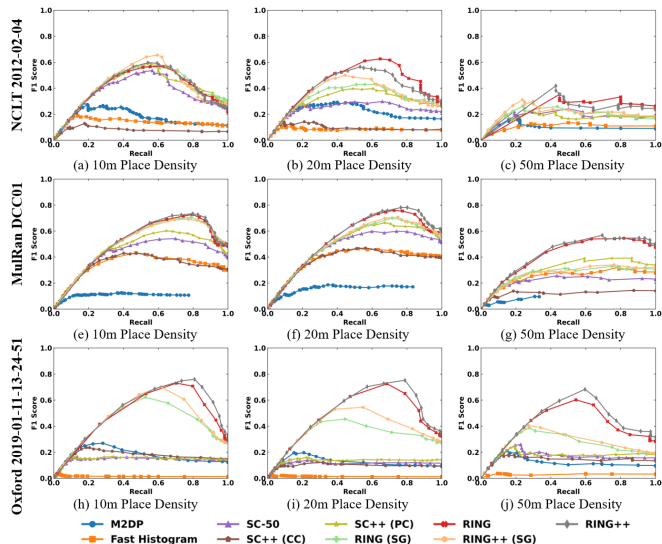


Fig. 9: F1 score-Recall Curve for NCLT, MulRan and Oxford datasets under single-session scenarios.

map sequence and query sequence respectively. Under multi-session scenarios, the sampling interval of query data is fixed to $5m$ for all datasets. In the same manner, we compare the proposed approach against the state-of-the-art methods at different map place density ($10m$, $20m$ and $50m$) on NCLT dataset, with the results depicted in Fig. 10. *Precision-Recall Curve* and *F1 score-Recall Curve* show the same trend as that in Fig. 8 and 9. RING (SG), RING++ (SG) and SC-based methods show competitive performance at high place density ($10m$) while RING and RING++ achieve better performance at low place density ($20m$ and $50m$) due to rigorous roto-translation invariance design. Using six extracted local features, RING++ (SG) and RING++ perform better than RING (SG) and RING, proving the validity of feature extraction for place recognition. To validate the cross-dataset consistency, we evaluate all methods on different datasets at $20m$ place density.

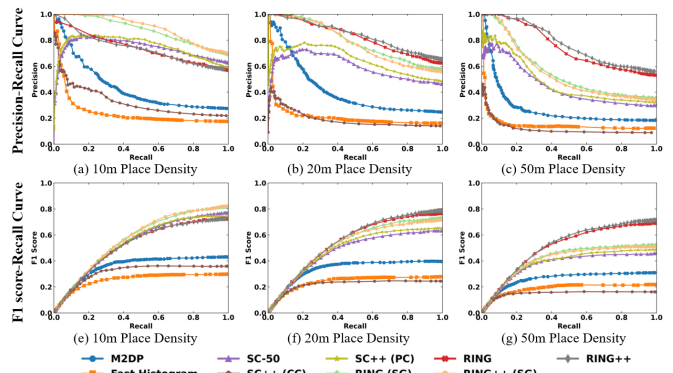


Fig. 10: Precision-Recall Curve (top) and F1 score-Recall Curve (bottom) for "2012-03-17" query sequence to "2012-02-04" map sequence in NCLT dataset.

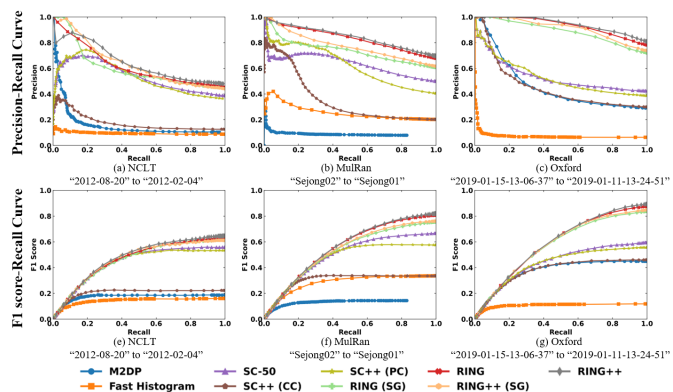


Fig. 11: Precision-Recall Curve (top) and F1 score-Recall Curve (bottom) for NCLT, MulRan and Oxford datasets at $20m$ place density.

Besides "2012-03-17" query sequence to "2012-02-04" map sequence for NCLT dataset, we perform long-term place recognition on "2012-08-20" to "2012-02-04" pair for NCLT dataset, "Sejong02" to "Sejong01" pair for MulRan dataset, and "2019-01-15-13-06-37" to "2019-01-11-13-24-51" pair for Oxford dataset, as shown in Fig. 11. Via comparison, four versions of our approach all outperform other approaches at $20m$ place density, especially for Oxford dataset, which presents the strength of roto-translation invariance for place recognition. In Fig. 12 and Fig. 13, we visualize the revisited pairs of *top1 retrieval* using different methods on NCLT and MulRan datasets at $20m$ place density. It can be easily seen that RING++ surpasses other methods by a lot, further validating the effectiveness of our approach in sparse places.

In addition to qualitative comparison, we provide the quantitative results of the handcrafted methods for long-term place recognition, as listed in Tab. II. Compared with other handcrafted methods, our method and its variants are capable of recognizing many more revisited places. Compared with RING (SG) and RING++ (SG), RING and RING++ make obvious improvements thanks to the translation invariance construction of RING representation based on TING.

3) *Generalization*: Unlike deep learning representations, our representation is training-free, so we can easily gener-

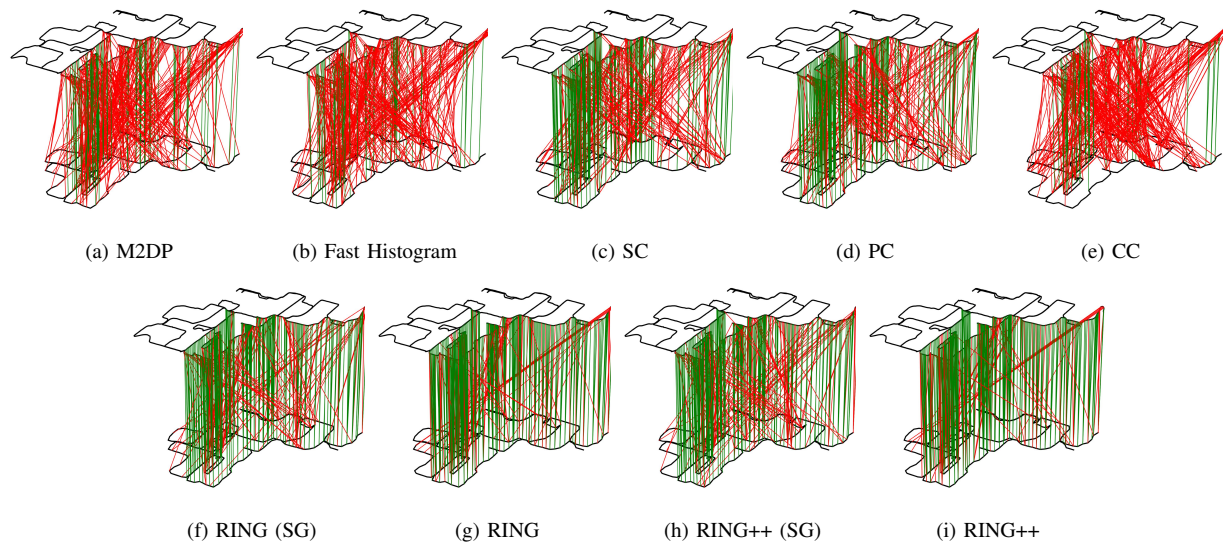


Fig. 12: Qualitative comparison of match graph for NCLT dataset at 20m place density, where black lines visualize trajectories, green lines visualize correctly retrieved pairs, and red lines visualize mistakenly retrieved pairs.

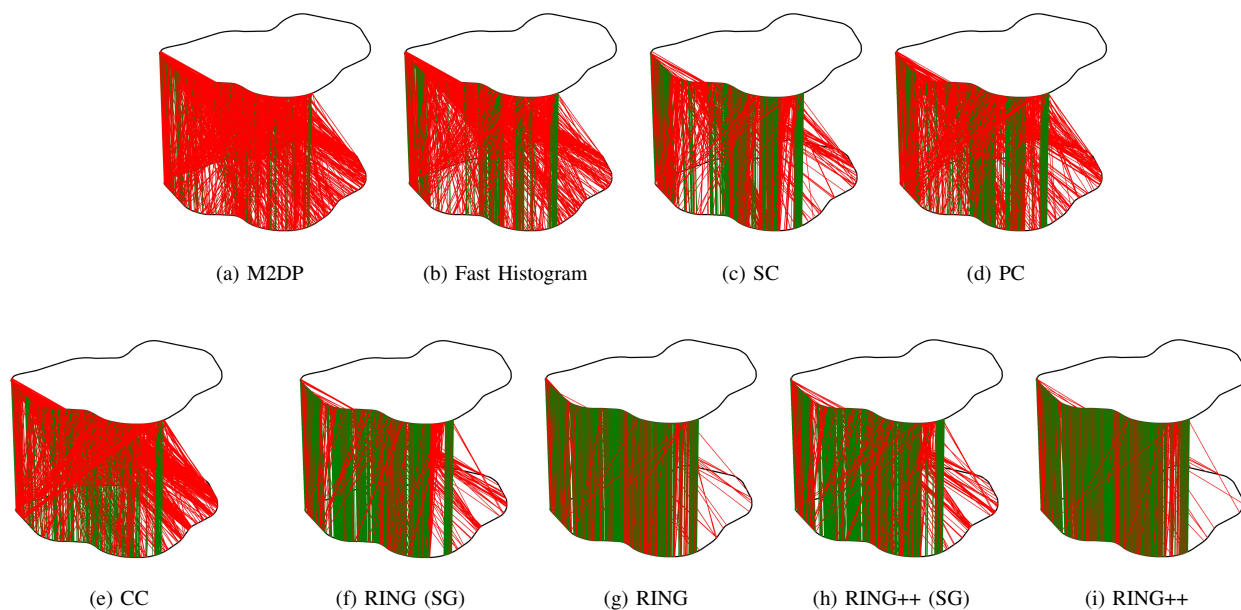


Fig. 13: Qualitative comparison of match graph for MulRan dataset at 20m place density, where black lines visualize trajectories, green lines visualize correctly retrieved pairs, and red lines visualize mistakenly retrieved pairs.

alize to new scenes without re-training or fine-tuning. We compare RING++ with some deep learning methods across different datasets to show our superior generalization ability among deep learning methods. For deep learning methods, we train the model on MulRan dataset (“Sejong01” trajectory serves as map sequence, “Sejong02” trajectory serves as query sequence) and validate it on NCLT dataset (“2012-02-04” trajectory serves as map sequence, “2012-03-17” trajectory serves as query sequence) and Oxford dataset (“2019-01-11-13-24-51” trajectory serves as map sequence, “2019-01-15-13-06-37” trajectory serves as query sequence) for generalization ability evaluation, where the equidistant sampling gap between

query data is $5m$ and that of map data is $20m$ with $10m$ revisited distance threshold.

As shown in Tab. III, RING++ has excellent performance across different datasets. DiSCO and EgoNN maintain most of their place recognition performance on generalized datasets due to their rotation invariant structures, but the polar transform still suffers from translation variance.

C. Evaluation of Pose Estimation

At the pose estimation stage, our method yields a 3-DoF pose: 1-DoF rotation and 2-DoF translation. We perform pose estimation on NCLT and MulRan datasets, which provides

TABLE II: Quantitative Results of Multi-session Scenarios

Dataset	Approach	Recall@1	F1 score	AUC
NCLT	RING++ (Ours)	0.7321	0.7890	0.8374
	RING++ (SG) (Ours)	0.6309	0.7150	0.7776
	RING (Ours)	<u>0.7098</u>	<u>0.7658</u>	<u>0.8246</u>
	RING (SG) (Ours)	0.6582	0.7274	0.7392
	M2DP	0.2811	0.3966	0.4127
	Fast Histogram	0.1840	0.2785	0.2136
	SC-50	0.5248	0.6314	0.5934
	SC++ (PC)	0.3862	0.6495	0.6465
	SC++ (CC)	0.1355	0.2449	0.1895
MulRan	RING++ (Ours)	0.7451	0.8267	0.8380
	RING++ (SG) (Ours)	0.6592	0.7625	0.7701
	RING (Ours)	<u>0.7256</u>	<u>0.8079</u>	<u>0.8329</u>
	RING (SG) (Ours)	0.6487	0.7549	0.7370
	M2DP	0.0831	0.1437	0.0750
	Fast Histogram	0.2163	0.3363	0.2551
	SC-50	0.5342	0.6658	0.6359
	SC++ (PC)	0.3740	0.6260	0.6260
	SC++ (CC)	0.1829	0.3347	0.3572
Oxford	RING++ (Ours)	0.8274	0.8937	0.9438
	RING++ (SG) (Ours)	0.7612	0.8492	0.8992
	RING (Ours)	<u>0.8013</u>	<u>0.8772</u>	<u>0.9234</u>
	RING (SG) (Ours)	0.7425	0.8366	0.8787
	M2DP	0.2997	0.4496	0.4638
	Fast Histogram	0.0642	0.1181	0.0741
	SC-50	0.4375	0.5935	0.5366
	SC++ (PC)	0.3993	0.5561	0.5295
	SC++ (CC)	0.3084	0.4596	0.4540

TABLE III: Generalization Evaluation*

Dataset	Approach	Recall@1	F1 score	AUC
MulRan*	RING++ (Ours)	0.6941	0.7983	0.8337
	PointNetVLAD	0.6968	0.8214	0.8436
	DiSCO	0.7425	0.8630	0.8973
	EgoNN	<u>0.7260</u>	<u>0.8412</u>	0.9060
NCLT	RING++ (Ours)	0.7321	0.7890	0.8374
	PointNetVLAD	0.3691	0.5391	0.6260
	DiSCO	<u>0.6036</u>	<u>0.7816</u>	0.7722
Oxford	EgoNN	0.5620	0.6965	<u>0.7988</u>
	RING++ (Ours)	0.8274	0.8937	0.9438
	PointNetVLAD	0.5247	0.7825	0.6114
	DiSCO	<u>0.6562</u>	<u>0.7890</u>	<u>0.8566</u>
EgoNN	0.5920	0.7438	0.8471	

* The compared learning-based methods are trained on MulRan dataset and evaluated on the other two datasets for generalization evaluation. For MulRan dataset, we perform place recognition evaluation on the test dataset which is used in EgoNN [40].

accurate 6-DoF ground truth poses. We utilize the same trajectories used in place recognition evaluation to compare the pose estimation performance for complete global localization evaluation.

We first compare the proposed four variants. The pose estimation error on “2012-03-17” to “2012-02-04” for NCLT dataset at different place density is visualized by box plot shown in Fig. 14. Together with pose estimation on NCLT dataset, we provide Tab. IV which presents *Success Rate*, *TE* and *RE* of our approach on “Sejong02” to “Sejong01” for MulRan dataset with a place density of 20m. As the results show, RING and RING++ estimate more accurate rotation

TABLE IV: Pose Estimation Error on MulRan Dataset*

Approach	MulRan		
	Success (%)	TE (m)	RE (°)
RING (SG)	53.01	0.58/1.08/4.52	0.51/1.77/5.94
RING	<u>63.47</u>	<u>0.51/0.70/1.81</u>	<u>0.35/0.73/1.52</u>
RING++ (SG)	53.01	0.60/1.17/4.54	0.62/2.54/6.24
RING++	65.76	0.50/0.70/1.79	0.34/0.72/1.51

* We list 50%, 75% and 95% quantiles of TE and RE in this table.

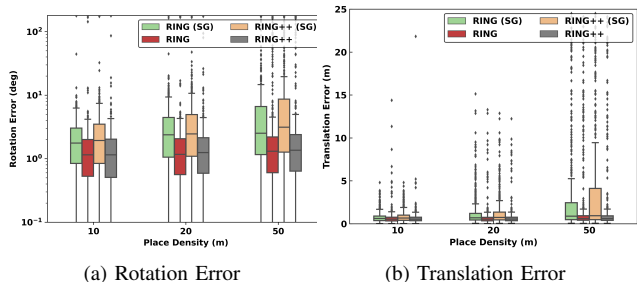


Fig. 14: Pose estimation error on NCLT dataset. (a) Relative 1-DoF rotation estimation error. (b) Relative 2-DoF translation estimation error.

and translation than RING (SG) and RING++ (SG), which indicates that translation invariance benefits pose estimation. By comparing RING with RING++, we find that the extracted six local features of RING++ do not obviously facilitate pose estimation performance. In general, RING++ performs the best among all variants.

To verify the quality of the 3-DoF pose estimated by our method, we employ ICP with and without the initial pose provided by the proposed method to align two matched scans after place recognition. The case results are illustrated in Fig. 15. As we can easily see, ICP fails without an initial guess, especially in the case of large rotation variance. Our approach offers a qualified initial guess for scan matching, close to the best alignment. With the estimated pose of RING++ (SG) and RING++, ICP converges to global minima rather than traps in local optima. Furthermore, the time cost of ICP with the initial guess is much less than without any initial poses.

After that, we compare RING++ with both handcrafted and learning-based methods on NCLT and MulRan datasets. For each dataset, we evaluate these approaches in terms of *Success Rate*, *TE* and *RE*. To demonstrate the effectiveness of better initial guesses, we also provide an additional pose estimation successful rate, which is calculated by the percentage of successfully aligned matches ($TE < 2m$ & $RE < 5^\circ$) among all correctly retrieved pairs.

1) *Comparison with Learning-free Methods*: Among the compared hand-engineering methods, M2DP and Fast Histogram are only capable of place recognition, while Scan Context and Scan Context++ produce 1-DoF relative pose (i.e., relative rotation or lateral translation) together with place recognition, leaving the remaining dimension to ICP. In contrast, our method yields a relative rotation that is a by-product in the process of place recognition and estimates

TABLE V: Quantitative Results of Pose Error Evaluation*

Approach	NCLT			MulRan			
	Success (%)	TE [†] (m)	RE [†] (°)	Success (%)	TE [†] (m)	RE [†] (°)	
Handcrafted	SC-50 + ICP	24.97/47.58	0.30/1.02/7.67	4.14/ 6.50/18.11	35.82/65.45	0.45/6.54/8.17	0.52/0.95/2.01
	SC++ (PC) + ICP	25.68/46.95	0.33/1.87/8.78	4.18/6.70/19.81	36.25/66.94	0.38/6.12/8.10	<u>0.51/0.94/1.96</u>
	SC++ (CC) + ICP	8.09/ <u>50.98</u>	0.36/14.30/139.55	3.67/7.06/177.01	18.19/62.23	0.48/138.85/140.63	0.47/0.80/1.48
Learning-based	DiSCO + ICP	<u>28.31/46.91</u>	0.35/2.73/8.73	6.09/ <u>6.52/34.69</u>	38.36/51.66	1.23/7.45/8.25	0.71/1.02/1.84
	EgoNN + ICP	6.07/10.80	3.48/8.12/15.51	12.32/27.45/134.95	<u>62.00/85.40</u>	<u>0.28/0.52/13.04</u>	0.72/1.14/1.98
Ours	RING++ + ICP	42.37/57.88	<u>0.31/0.53/1.36</u>	<u>4.13/6.74/12.52</u>	66.09/95.22	0.27/0.42/1.82	<u>0.51/0.80/1.19</u>

[†] As ICP refinement is applied, TE here represents 3-DoF translation error and RE represents 3-DoF rotation error.

* We list 50%, 75% and 95% quantiles of TE and RE in this table. The second value of *Success Rate* is the percentage of successfully aligned matches ($TE < 2m$ & $RE < 5^\circ$) among all correctly retrieved pairs. For MulRan dataset, we perform place recognition and pose estimation evaluation on the test dataset which is used in EgoNN [40].

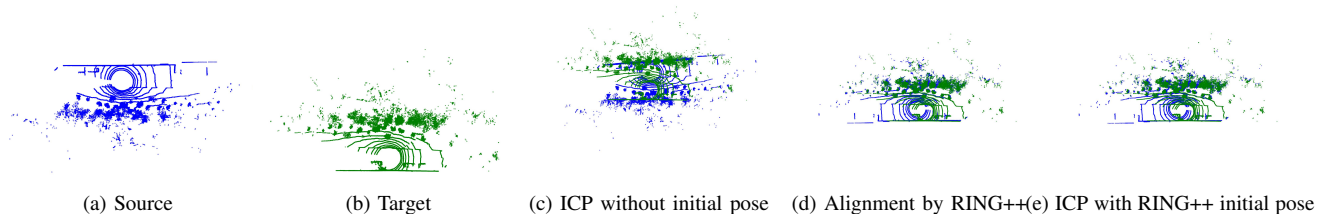


Fig. 15: ICP alignment with and without initial pose provided by RING++.

a 2-DoF relative translation successively in the process of pose estimation. For fair comparison, we evaluate the pose estimation performance of all methods after refinement by ICP. As can be seen in Tab. V, we calculate *Success Rate* for global localization evaluation and *TE* and *RE* at 50%, 75% and 95% for pose estimation evaluation. Compared with SC-based methods, RING++ has better performance on both NCLT and MulRan datasets, arriving at high *Success Rate* for global localization. Referring to the pose estimation success rate, RING++ has a better chance of achieving satisfied alignment by providing the qualified 3-DoF initial guesses, which makes refinement more easily converge to the global optimal pose. Our method achieves less *TE* and *RE* at most quantiles, which verifies the efficacy of better initial guesses.

2) *Comparison with Learning-based Methods:* Learning-based methods, DiSCO and EgoNN, are trained on MulRan dataset and tested on both MulRan and NCLT datasets for generalization evaluation. For MulRan dataset, EgoNN shows great performance of pose estimation thanks to the extracted local features. RING++ presents competitive performance (66.09% *Success Rate*) to EgoNN (62.00% *Success Rate*). The overall global localization is mainly limited by the place recognition performance which we discuss in the Section VII-F. In terms of pose estimation error, RING++ has lower *TE* and *RE* than DiSCO and EgoNN. For NCLT dataset, the distribution of points is different from that of MulRan dataset due to the different LiDAR sensor, which makes it hard for generalization. Therefore, the global localization performance of learning-based methods on NCLT dataset drops a lot, especially for EgoNN. The underlying reason may be explained by the lack of explicit invariance design in EgoNN, making the feature correlated and fail to generalize to unseen datasets.

TABLE VI: Ablation Study on the Resolution*

Resolution	Recall@1 (%)	TE (m)	RE (°)
40×40 (3.50 m, 9°)	62.18	1.43/2.08/3.73	2.45/4.14/7.27
60×60 (2.33 m, 6°)	68.76	0.98/1.37/2.52	1.86/3.19/5.96
80×80 (1.75 m, 4.5°)	71.59	0.79/1.10/1.95	1.53/2.70/5.32
120×120 (1.17 m, 3°)	73.21	0.56/0.77/1.31	1.25/2.14/4.07
160×160 (0.88 m, 2.25°)	75.83	0.48/0.70/1.30	1.08/1.98/3.59
200×200 (0.70 m, 1.8°)	76.54	0.41/0.60/1.10	1.08/1.93/3.26
300×300 (0.47 m, 1.2°)	77.65	0.32/0.48/1.13	1.07/1.79/3.13

* We list 50%, 75% and 95% quantiles of TE and RE in this table.

Unlike EgoNN, DiSCO constructs a rotation invariant place descriptor by transforming features to the frequency domain and then taking the magnitude of the frequency spectrum, which explains the relatively smaller decline of *Success Rate* value from MulRan dataset generalizing to NCLT dataset. Through comparison, RING++, as a learning-free method arrives at the top performance on NCLT dataset, with high *Success Rate* and small *TE* and *RE*.

D. Ablation Study

To investigate the influence of resolution on place recognition and pose estimation, we present ablation studies on the grid size and corresponding resolution of RING++. We carry out experiments utilizing the same multi-session pair

TABLE VII: Ablation Study on Local Features*

Local Features	Recall@1 (%)	TE (m)	RE (°)
FPFH [35] w/ RING++	75.03	0.56/0.79/1.30	1.19/2.03/4.03
SHOT [19] w/ RING++	63.73	0.56/0.79/1.39	1.16/2.03/4.08

* We list 50%, 75% and 95% quantiles of TE and RE in this table.

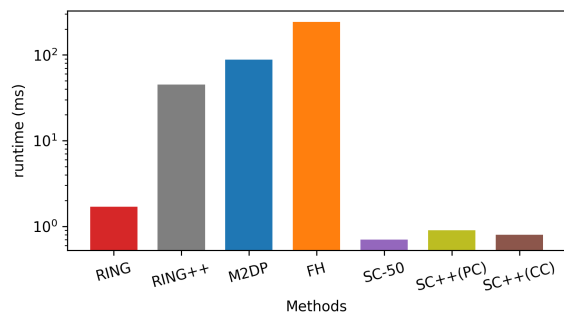


Fig. 16: Average computational time when tested on NCLT Dataset. FH represents Fast Histogram.

“2012-03-17” to “2012-02-04” in NCLT dataset, with the results displayed in Tab. VI. As the grid size/resolution increases, *Recall@1* of our method increases fast at first and then approaches a constant gradually. Additionally, translation estimation error declines slightly, while rotation estimation benefits greatly from the increased resolution.

The other ablation study is carried out to confirm RING++’s effectiveness as a feature aggregation method. Using the same multi-session pair from the NCLT dataset, we test RING++ using several local features with the resolution set to 120×120 . The results are shown in Tab. VII. We utilize FPFH [35] implemented in Open3D [57], which extracts 33-channel point features. Regarding SHOT [18], [19], we use its Python implementation and change the bin value to 2, which results in the final 64-channel features. Although the bin value can be increased to 11 as in the original work, we only set it to 2 because of the linear memory consumption growth during the evaluation. The results show that our RING++ can also perform well with only two signature bins. Compared to the features we selected, FPFH and SHOT show competitive performance, validating the RING++ framework as a generic feature aggregation method. To strike a balance between precision and storage, we use 6-channel features introduced in Section V-A in all other experiments.

E. Computational Cost

Considering the real-time constraint, we calculate the computation cost of our algorithm. All methods are implemented in Python and tested on a system equipped with an Intel i7-10700 (2.9GHz) and an Nvidia GeForce RTX 2060 SUPER with 8G memory. As can be seen in Fig. 16, the average computational time of RING++ is less than 50ms. The most time-consuming part is the calculation of local features. It is worth noting that the time consumption varies according to

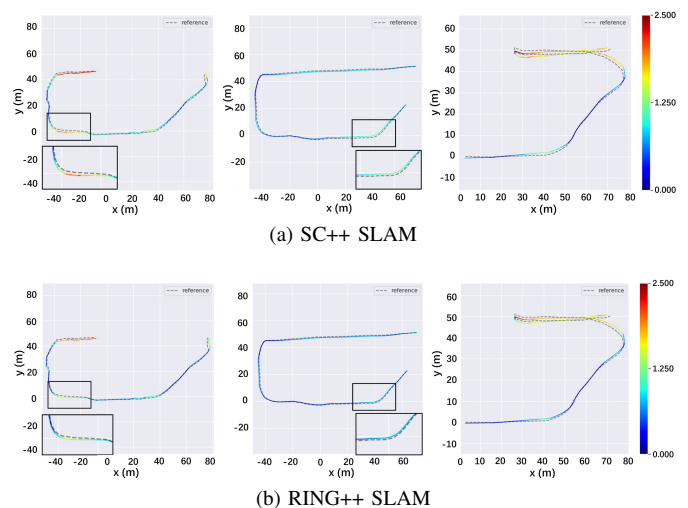


Fig. 17: Error visualization of Scan Context++ (PC) integrated SLAM system (top) compared to our approach (bottom) on legged robot dataset.

the number of channels in the local feature. It grows linearly as the feature channel increases.

F. Limitations and Potential Extension

1) *Limited Evaluation Performance*: RING++ can retrieve places with large viewpoint differences thanks to its roto-translation invariance property. As a result, the retrieved places may not be close enough to satisfy revisited criteria during evaluation, leading to a reduced place recognition success rate. However, in real-world applications, the success rate of place recognition is not a primary goal. Despite the fact that some of the retrieved places are not close to the current one, our estimators can provide satisfactory initial poses, resulting in improved overall global localization performance.

2) *Leveraging Deep learning for Feature Extraction*: We utilize handcrafted local features to validate our multi-channel framework; however, the representation ability of these features is limited. To achieve better performance, a possible way is to utilize learning-based local features with an end-to-end learning framework that takes RING++ as an aggregation.

VIII. SYSTEM APPLICATION

As a lightweight framework, we implement the proposed RING++ into a stand-alone module without any prior information. We also integrate a real-time back-end manager with the pose graph optimizer implemented by GTSAM [58]. With the optimization results acquired, we rearrange the keyframes to generate a global map. These components, together with any front-end odometry, can form a complete SLAM system. To validate the performance of our approach in real-world applications, we integrate FAST-LIO2 [59] into our SLAM system and compare RING++ and Scan context++ (PC) within this SLAM system.

A. Multi-robot SLAM System

In real applications such as exploration and rescue, multi-robot SLAM systems are expected to quickly build a precise

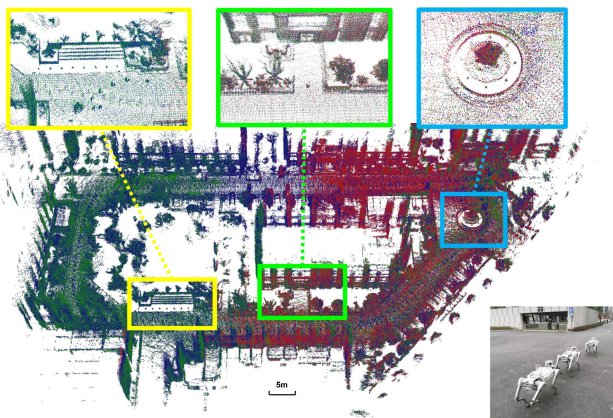


Fig. 18: Qualitative results of our RING++ SLAM on legged robot dataset. Different colored points are generated from different legged robots.

TABLE VIII: ATE and successfully aligned loop number of Scan Context++ (PC) and RING++ integrated SLAM systems.

Approach	Legged Robot Dataset		NCLT	
	ATE (m)	Succ. Loop	ATE (m)	Succ. Loop
SC++ SLAM	1.56	151	7.89	66
RING++ SLAM	0.72	167	6.43	126

environment map. The precision of the map is largely dependent on the correct alignment between keyframes. Because of the motion flexibility, legged robots are frequently used in such scenarios [60]. With this background, we collected data from three legged robots outfitted with an IMU-integrated Ouster64 LiDAR and a Jetson Xavier NX. The ground truth is acquired by the offline interactive SLAM [61] with automatically added and handpicked edges. In this setup, keyframes are generated at $2m$ intervals. The results are shown in Tab. VIII and Fig. 17, RING++ provides more successfully aligned loops for back-end pose optimization, which leads to lower drifts. The point cloud built by our system can be seen in Fig. 18, points generated by different robots are well aligned.

B. Multi-session SLAM System

Another application of RING++ is multi-session SLAM. It differs from multi-robot SLAM system in the changing of environment. The chosen NCLT dataset contains a wide range of environmental changes, such as dynamic objects, seasonal changes like winter and summer, and structural changes like building construction. We evaluate our system on “2012-05-26” and “2012-03-17”. The data from these sessions is processed online at the same time, indicating a multi-robot setup. The LiDAR points replayed online are from different sessions, forming a challenging temporal/spatial multi-agent setup. To maintain a sparse representation for the very large environment, we generate keyframes at $5m$ intervals. The performance can be seen in Tab. VIII and Fig. 19, RING++ provides almost twice the number of loop closures than Scan Context++ (PC), thus has better performance. The mapping result is shown in Fig. 20, where two different colored points represent two NCLT dataset sequences. The overlapping

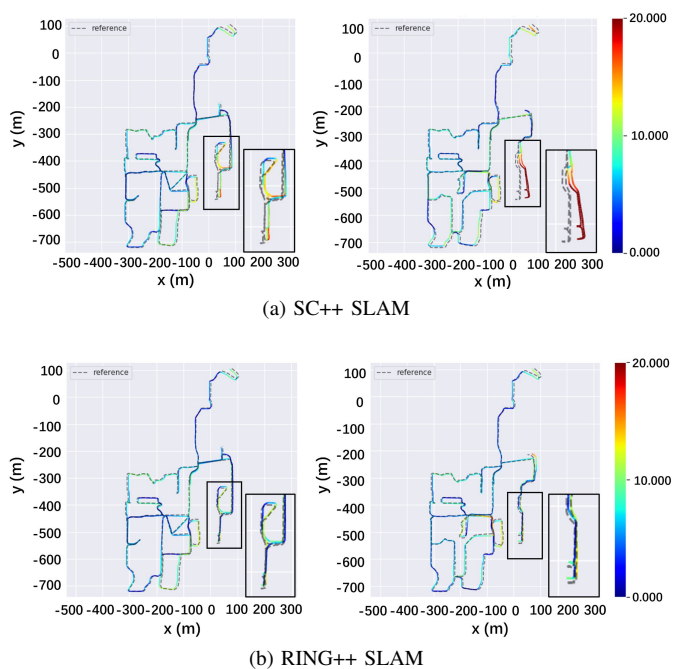


Fig. 19: Error visualization of Scan Context++ (PC) integrated SLAM system (top) compared to our approach (bottom) on two sequences of NCLT dataset. (left: “2012-05-26”, right: “2012-03-17”)

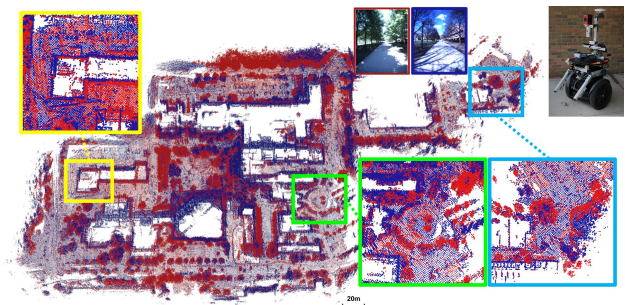


Fig. 20: Qualitative results of our RING++ SLAM on NCLT Dataset. Red points are generated from “2012-05-26” while blue points are generated from “2012-03-17”.

landmarks in magnified figures indicate the low drift of our system. It should be noted that FAST-LIO2 failed to provide acceptable odometry in the final minutes of the NCLT dataset, so those parts were discarded in the evaluation.

IX. CONCLUSION

In this paper, we present a roto-translation invariant framework RING++ for global localization on the sparse scan map, including representation pass and solving pass. Specifically, we extract six local features with geometry information and aggregate the features into three representations in the representation pass: rotation equivariant SG, translation invariant and rotation equivariant TING, and roto-translation invariant RING. In the solving pass, we perform place recognition, rotation estimation, translation estimation, and pose refinement. Thanks to roto-translation invariant representation, RING++

achieves superior performance on benchmark datasets, outperforming the state-of-the-art methods. By integrating RING++ as a stand-alone loop closure detection module into SLAM systems, we validate the effectiveness of our approach without any prior knowledge in real scenarios.

APPENDIX A PROOF OF EQ. 19

After normalizing TING M to \tilde{M} with a mean of 0 and a standard deviation of 1, the resultant \tilde{M} can be written as:

$$\tilde{M} = \frac{M - \mu(M)}{\sigma(M)} \quad (38)$$

where $\mu(M)$ is the mean of M , and $\sigma(M)$ is the standard deviation of M .

Then the resultant RING element $\tilde{N}_{Q,i}$ based on normalized \tilde{M}_Q and \tilde{M}_i is

$$\begin{aligned} \tilde{N}_{Q,i} &= \max_{k_\theta} \tilde{\mathcal{C}}_i(k_\theta) \\ &= \max_{k_\theta} \sum_{\theta_j} \tilde{M}_Q(\theta_j + k_\theta) \tilde{M}_i(\theta_j)^T \end{aligned} \quad (39)$$

Substituting Eq. 39 into Eq. 19, we have:

$$\begin{aligned} n &= \arg \max_i \tilde{N}_{Q,i} \\ &= \arg \max_i (\max_{k_\theta} \sum_{\theta_j} \tilde{M}_Q(\theta_j + k_\theta) \tilde{M}_i(\theta_j)^T) \end{aligned} \quad (40)$$

For efficient place retrieval leveraging Eq. 19, we need to prove that Eq. 19 is mathematically equivalent to Eq. 18. Since the length l of RING descriptor varies with the number of map scans, we begin with the proof at the simplest case $l = 2$. With $l = 2$, let $\tilde{N}_Q = (s_1, s_2)$, so $\tilde{N}_{Q,1} = s_1$ and $\tilde{N}_{Q,2} = s_2$. Suppose \tilde{N}_{i_1} is the RING descriptor of the first map scan and \tilde{N}_{i_2} is that of the second map scan. Due to normalization, we can easily conclude that $s_1 \leq 1$ and $s_2 \leq 1$ according to Eq. 39. In terms of \tilde{N}_{i_1} and \tilde{N}_{i_2} , we have $\tilde{N}_{i_1,1} = \tilde{N}_{i_2,2} = 1$ because of auto-correlation:

$$\begin{aligned} \tilde{N}_{i,i} &= \max_{k_\theta} \sum_{\theta_j} \tilde{M}_i(\theta_j + k_\theta) \tilde{M}_i(\theta_j)^T \\ &= \sum_{\theta_j} \tilde{M}_i(\theta_j) \tilde{M}_i(\theta_j)^T \\ &= |\tilde{M}_i|^2 = 1 \end{aligned} \quad (41)$$

Supposing $\tilde{N}_{i_1} = (1, k)$ where $k < 1$ since the two map scans are different, then $\tilde{N}_{i_2} = (k, 1)$. In this case, the problem turns to prove that $\|\tilde{N}_Q - \tilde{N}_{i_1}\| < \|\tilde{N}_Q - \tilde{N}_{i_2}\|$ if and only if $\tilde{N}_{Q,1} > \tilde{N}_{Q,2}$, which involves two sub-proofs: sufficiency proof and necessity proof.

Proof of Sufficiency: We begin with proof of sufficiency. The Euclidean distance between \tilde{N}_Q and \tilde{N}_{i_1} , \tilde{N}_{i_2} is formulated as:

$$\begin{aligned} \|\tilde{N}_Q - \tilde{N}_{i_1}\| &= (s_1 - 1)^2 + (s_2 - k)^2 \\ \|\tilde{N}_Q - \tilde{N}_{i_2}\| &= (s_1 - k)^2 + (s_2 - 1)^2 \end{aligned}$$

If $\tilde{N}_{Q,1} > \tilde{N}_{Q,2}$, that is $s_1 > s_2$, then we have:

$$\|\tilde{N}_Q - \tilde{N}_{i_1}\| - \|\tilde{N}_Q - \tilde{N}_{i_2}\| = 2(k - 1)(s_1 - s_2) < 0$$

Thus, if $\tilde{N}_{Q,1} > \tilde{N}_{Q,2}$, $\|\tilde{N}_Q - \tilde{N}_{i_1}\| < \|\tilde{N}_Q - \tilde{N}_{i_2}\|$.

Proof of Necessity: After that, we embark on proof of the necessity. If $\|\tilde{N}_Q - \tilde{N}_{i_1}\| < \|\tilde{N}_Q - \tilde{N}_{i_2}\|$, we have:

$$\|\tilde{N}_Q - \tilde{N}_{i_1}\| - \|\tilde{N}_Q - \tilde{N}_{i_2}\| = 2(k - 1)(s_1 - s_2) < 0$$

Since $k < 1$, then we arrive at:

$$s_1 > s_2$$

Thus, if $\|\tilde{N}_Q - \tilde{N}_{i_1}\| < \|\tilde{N}_Q - \tilde{N}_{i_2}\|$, $\tilde{N}_{Q,1} > \tilde{N}_{Q,2}$.

Therefore, we conclude that Eq. 18 holds if and only if Eq. 19 holds.

APPENDIX B PROOF OF FAST IMPLEMENTATION BY FFT

In order to fasten the computation of circular cross-correlation employed in RING formation, we take advantage of parallelized fast Fourier transform (FFT) to efficiently carry out cross-correlation. To be more specific, we apply DFT along θ axis of TING M_Q and M_i for all $\omega \triangleq \{\omega_m\}$, resulting in the frequency spectrum $F_Q(u, \omega_m)$ and $F_n(u, \omega_m)$:

$$\begin{aligned} F_Q(u, \omega_m) &= \mathcal{F}(M_Q(\theta, \omega_m)) = \sum_{\theta_j} M_Q(\theta_j, \omega_m) e^{-i2\pi u \frac{j}{l}} \\ F_n(u, \omega_m) &= \mathcal{F}(M_n(\theta, \omega_m)) = \sum_{\theta_j} M_n(\theta_j, \omega_m) e^{-i2\pi u \frac{j}{l}} \end{aligned} \quad (42)$$

where u is the discrete frequency of the frequency spectrum. After that, we multiply $F_Q(u, \omega_m)$ by the complex conjugate of $F_n(u, \omega_m)$ and then employ inverse Fourier transform (IFT) to obtain a 2D correlation map $\mathcal{C}_i(k_\theta, k_\omega)$:

$$\begin{aligned} \mathcal{C}_i(k_\theta, k_\omega) &= \mathcal{F}^{-1}(F_Q(u, \omega_m) F_n^*(u, \omega_m)) \\ &= \sum_{\theta_j} \sum_{\omega_m} M_Q(\theta_j + k_\theta, \omega_m + k_\omega) M_i(\theta_j, \omega_m) \end{aligned} \quad (43)$$

By summing along k_ω axis of the correlation map, we can obtain the resultant 1D correlation map $\mathcal{C}_i(k_\theta)$ of 1D circular cross-correlation on 2D image defined in this paper:

$$\begin{aligned} \mathcal{C}_i(k_\theta) &= \sum_{\theta_j} \sum_{\omega_m} M_Q(\theta_j + k_\theta, \omega_m) M_i(\theta_j, \omega_m) \\ &= \sum_{\theta_j} M_Q(\theta_j + k_\theta) M_i(\theta_j)^T \end{aligned} \quad (44)$$

REFERENCES

- [1] C. Valgren and A. J. Lilienthal, "Sift, surf and seasons: Long-term outdoor localization using local features," in *3rd European conference on mobile robots, ECMR'07, Freiburg, Germany, September 19-21, 2007*, 2007, pp. 253–258.
- [2] S. Lowry, N. Sünderhauf, P. Newman, J. J. Leonard, D. Cox, P. Corke, and M. J. Milford, "Visual place recognition: A survey," *IEEE Transactions on Robotics*, vol. 32, no. 1, pp. 1–19, 2015.
- [3] G. Kim and A. Kim, "Scan context: Egocentric spatial descriptor for place recognition within 3d point cloud map," in *2018 IEEE/RSJ International Conference on Intelligent Robots and Systems (IROS)*. IEEE, 2018, pp. 4802–4809.

- [4] Y. Wang, Z. Sun, C.-Z. Xu, S. E. Sarma, J. Yang, and H. Kong, "Lidar iris for loop-closure detection," in *2020 IEEE/RSJ International Conference on Intelligent Robots and Systems (IROS)*. IEEE, 2020, pp. 5769–5775.
- [5] K. Vidanapathirana, P. Moghadam, B. Harwood, M. Zhao, S. Sridharan, and C. Fookes, "Locus: Lidar-based place recognition using spatiotemporal higher-order pooling," in *2021 IEEE International Conference on Robotics and Automation (ICRA)*, 2021, pp. 5075–5081.
- [6] J. Komorowski, "Minkloc3d: Point cloud based large-scale place recognition," in *Proceedings of the IEEE/CVF Winter Conference on Applications of Computer Vision*, 2021, pp. 1790–1799.
- [7] T. Röhling, J. Mack, and D. Schulz, "A fast histogram-based similarity measure for detecting loop closures in 3-d lidar data," in *2015 IEEE/RSJ International Conference on Intelligent Robots and Systems (IROS)*. IEEE, 2015, pp. 736–741.
- [8] L. He, X. Wang, and H. Zhang, "M2dp: A novel 3d point cloud descriptor and its application in loop closure detection," in *2016 IEEE/RSJ International Conference on Intelligent Robots and Systems (IROS)*. IEEE, 2016, pp. 231–237.
- [9] M. A. Uy and G. H. Lee, "Pointnetvlad: Deep point cloud based retrieval for large-scale place recognition," in *Proceedings of the IEEE conference on computer vision and pattern recognition*, 2018, pp. 4470–4479.
- [10] Z. Liu, S. Zhou, C. Suo, P. Yin, W. Chen, H. Wang, H. Li, and Y.-H. Liu, "Lpd-net: 3d point cloud learning for large-scale place recognition and environment analysis," in *Proceedings of the IEEE/CVF International Conference on Computer Vision*, 2019, pp. 2831–2840.
- [11] G. Kim, S. Choi, and A. Kim, "Scan context++: Structural place recognition robust to rotation and lateral variations in urban environments," *IEEE Transactions on Robotics*, 2021.
- [12] S. Lu, X. Xu, H. Yin, R. Xiong, and Y. Wang, "One ring to rule them all: Radon sinogram for place recognition, orientation and translation estimation," *arXiv preprint arXiv:2204.07992*, 2022.
- [13] F. Stein, G. Medioni, et al., "Structural indexing: Efficient 3-d object recognition," *IEEE Transactions on Pattern Analysis and Machine Intelligence*, vol. 14, no. 2, pp. 125–145, 1992.
- [14] R. B. Rusu, N. Blodow, Z. C. Marton, and M. Beetz, "Aligning point cloud views using persistent feature histograms," in *2008 IEEE/RSJ international conference on intelligent robots and systems*. IEEE, 2008, pp. 3384–3391.
- [15] M. Weinmann, B. Jutzi, and C. Mallet, "Semantic 3d scene interpretation: A framework combining optimal neighborhood size selection with relevant features," *ISPRS Annals of the Photogrammetry, Remote Sensing and Spatial Information Sciences*, vol. 2, no. 3, p. 181, 2014.
- [16] A. E. Johnson and M. Hebert, "Using spin images for efficient object recognition in cluttered 3d scenes," *IEEE Transactions on pattern analysis and machine intelligence*, vol. 21, no. 5, pp. 433–449, 1999.
- [17] W. Wohlkinger and M. Vincze, "Ensemble of shape functions for 3d object classification," in *2011 IEEE international conference on robotics and biomimetics*. IEEE, 2011, pp. 2987–2992.
- [18] F. Tombari, S. Salti, and L. Di Stefano, "A combined texture-shape descriptor for enhanced 3d feature matching," in *2011 18th IEEE international conference on image processing*. IEEE, 2011, pp. 809–812.
- [19] F. Tombari, S. Salti, and L. di Stefano, "Shot: Unique signatures of histograms for surface and texture description," *Computer Vision and Image Understanding*, vol. 125, pp. 251–264, 2014. [Online]. Available: <https://www.sciencedirect.com/science/article/pii/S1077314214000988>
- [20] D. Maturana and S. Scherer, "Voxnet: A 3d convolutional neural network for real-time object recognition," in *2015 IEEE/RSJ international conference on intelligent robots and systems (IROS)*. IEEE, 2015, pp. 922–928.
- [21] Z. Wu, S. Song, A. Khosla, F. Yu, L. Zhang, X. Tang, and J. Xiao, "3d shapenets: A deep representation for volumetric shapes," in *Proceedings of the IEEE conference on computer vision and pattern recognition*, 2015, pp. 1912–1920.
- [22] Y. Zhou and O. Tuzel, "Voxelnet: End-to-end learning for point cloud based 3d object detection," in *Proceedings of the IEEE conference on computer vision and pattern recognition*, 2018, pp. 4490–4499.
- [23] C. R. Qi, H. Su, K. Mo, and L. J. Guibas, "Pointnet: Deep learning on point sets for 3d classification and segmentation," in *Proceedings of the IEEE conference on computer vision and pattern recognition*, 2017, pp. 652–660.
- [24] C. R. Qi, L. Yi, H. Su, and L. J. Guibas, "Pointnet++: Deep hierarchical feature learning on point sets in a metric space," *Advances in neural information processing systems*, vol. 30, 2017.
- [25] Y. Wang, Y. Sun, Z. Liu, S. E. Sarma, M. M. Bronstein, and J. M. Solomon, "Dynamic graph cnn for learning on point clouds," *Acm Transactions On Graphics (tog)*, vol. 38, no. 5, pp. 1–12, 2019.
- [26] Y. Shen, C. Feng, Y. Yang, and D. Tian, "Mining point cloud local structures by kernel correlation and graph pooling," in *Proceedings of the IEEE conference on computer vision and pattern recognition*, 2018, pp. 4548–4557.
- [27] X. Chen, T. Labe, A. Milioto, T. Röhling, O. Vysotska, A. Haag, J. Behley, and C. Stachniss, "Overlapnet: Loop closing for lidar-based slam," *arXiv preprint arXiv:2105.11344*, 2021.
- [28] L. Li, X. Kong, X. Zhao, T. Huang, W. Li, F. Wen, H. Zhang, and Y. Liu, "Ssc: Semantic scan context for large-scale place recognition," in *2021 IEEE/RSJ International Conference on Intelligent Robots and Systems (IROS)*. IEEE, 2021, pp. 2092–2099.
- [29] J. Komorowski, M. Wysoczańska, and T. Trzcinski, "Minkloc++: lidar and monocular image fusion for place recognition," in *2021 International Joint Conference on Neural Networks (IJCNN)*. IEEE, 2021, pp. 1–8.
- [30] Y. Pan, X. Xu, W. Li, Y. Cui, Y. Wang, and R. Xiong, "Coral: Colored structural representation for bi-modal place recognition," in *2021 IEEE/RSJ International Conference on Intelligent Robots and Systems (IROS)*. IEEE, 2021, pp. 2084–2091.
- [31] H. Lai, P. Yin, and S. Scherer, "Adafusion: Visual-lidar fusion with adaptive weights for place recognition," *arXiv preprint arXiv:2111.11739*, 2021.
- [32] J. Knopp, M. Prasad, G. Willems, R. Timofte, and L. V. Gool, "Hough transform and 3d surf for robust three dimensional classification," in *European Conference on Computer Vision*. Springer, 2010, pp. 589–602.
- [33] H. Bay, T. Tuytelaars, and L. V. Gool, "Surf: Speeded up robust features," in *European conference on computer vision*. Springer, 2006, pp. 404–417.
- [34] R. B. Rusu, N. Blodow, and M. Beetz, "Fast point feature histograms (fpfh) for 3d registration," in *2009 IEEE international conference on robotics and automation*. IEEE, 2009, pp. 3212–3217.
- [35] R. B. Rusu, G. Bradski, R. Thibaux, and J. Hsu, "Fast 3d recognition and pose using the viewpoint feature histogram," in *2010 IEEE/RSJ International Conference on Intelligent Robots and Systems*. IEEE, 2010, pp. 2155–2162.
- [36] R. Arandjelovic, P. Gronat, A. Torii, T. Pajdla, and J. Sivic, "Netvlad: Cnn architecture for weakly supervised place recognition," in *Proceedings of the IEEE conference on computer vision and pattern recognition*, 2016, pp. 5297–5307.
- [37] H. Jégou, M. Douze, C. Schmid, and P. Pérez, "Aggregating local descriptors into a compact image representation," in *2010 IEEE computer society conference on computer vision and pattern recognition*. IEEE, 2010, pp. 3304–3311.
- [38] X. Xu, H. Yin, Z. Chen, Y. Li, Y. Wang, and R. Xiong, "Disco: Differentiable scan context with orientation," *IEEE Robotics and Automation Letters*, vol. 6, no. 2, pp. 2791–2798, 2021.
- [39] K. Żywanowski, A. Banaszczyk, M. R. Nowicki, and J. Komorowski, "Minkloc3d-si: 3d lidar place recognition with sparse convolutions, spherical coordinates, and intensity," *IEEE Robotics and Automation Letters*, vol. 7, no. 2, pp. 1079–1086, 2021.
- [40] J. Komorowski, M. Wysoczanska, and T. Trzcinski, "Egonn: Egocentric neural network for point cloud based 6dof relocalization at the city scale," *IEEE Robotics and Automation Letters*, vol. 7, no. 2, pp. 722–729, 2021.
- [41] F. Radenović, G. Tolia, and O. Chum, "Fine-tuning cnn image retrieval with no human annotation," *IEEE transactions on pattern analysis and machine intelligence*, vol. 41, no. 7, pp. 1655–1668, 2018.
- [42] H. Yin, L. Tang, X. Ding, Y. Wang, and R. Xiong, "Locnet: Global localization in 3d point clouds for mobile vehicles," in *2018 IEEE Intelligent Vehicles Symposium (IV)*. IEEE, 2018, pp. 728–733.
- [43] X. Ding, X. Xu, S. Lu, Y. Jiao, M. Tan, R. Xiong, H. Deng, M. Li, and Y. Wang, "Translation invariant global estimation of heading angle using sinogram of lidar point cloud," *arXiv preprint arXiv:2203.00924*, 2022.
- [44] W. Lu, Y. Zhou, G. Wan, S. Hou, and S. Song, "L3-net: Towards learning based lidar localization for autonomous driving," in *Proceedings of the IEEE/CVF Conference on Computer Vision and Pattern Recognition (CVPR)*, June 2019.
- [45] P. J. Besl and N. D. McKay, "Method for registration of 3-d shapes," in *Sensor fusion IV: control paradigms and data structures*, vol. 1611. Spie, 1992, pp. 586–606.

- [46] I. Sipiran and B. Bustos, "Harris 3d: a robust extension of the harris operator for interest point detection on 3d meshes," *The Visual Computer*, vol. 27, no. 11, pp. 963–976, 2011.
- [47] R. Arandjelovic and A. Zisserman, "All about vlad," in *Proceedings of the IEEE conference on Computer Vision and Pattern Recognition*, 2013, pp. 1578–1585.
- [48] P. Scovanner, S. Ali, and M. Shah, "A 3-dimensional sift descriptor and its application to action recognition," in *Proceedings of the 15th ACM international conference on Multimedia*, 2007, pp. 357–360.
- [49] N. Carlevaris-Bianco, A. K. Ushani, and R. M. Eustice, "University of michigan north campus long-term vision and lidar dataset," *The International Journal of Robotics Research*, vol. 35, no. 9, pp. 1023–1035, 2016.
- [50] G. Kim, Y. S. Park, Y. Cho, J. Jeong, and A. Kim, "Mulran: Multimodal range dataset for urban place recognition," in *2020 IEEE International Conference on Robotics and Automation (ICRA)*. IEEE, 2020, pp. 6246–6253.
- [51] D. Barnes, M. Gadd, P. Murcutt, P. Newman, and I. Posner, "The oxford radar robotcar dataset: A radar extension to the oxford robotcar dataset," in *2020 IEEE International Conference on Robotics and Automation (ICRA)*. IEEE, 2020, pp. 6433–6438.
- [52] W. Maddern, G. Pascoe, C. Linegar, and P. Newman, "1 year, 1000 km: The oxford robotcar dataset," *The International Journal of Robotics Research*, vol. 36, no. 1, pp. 3–15, 2017.
- [53] V. Raghavan, P. Bollmann, and G. S. Jung, "A critical investigation of recall and precision as measures of retrieval system performance," *ACM Transactions on Information Systems (TOIS)*, vol. 7, no. 3, pp. 205–229, 1989.
- [54] D. M. Christopher and S. Hinrich, "Foundations of statistical natural language processing," 1999.
- [55] H. Schütze, C. D. Manning, and P. Raghavan, *Introduction to information retrieval*. Cambridge University Press Cambridge, 2008, vol. 39.
- [56] D. Cattaneo, M. Vaghi, and A. Valada, "Lednet: Deep loop closure detection for lidar slam based on unbalanced optimal transport," 2021.
- [57] Q.-Y. Zhou, J. Park, and V. Koltun, "Open3D: A modern library for 3D data processing," *arXiv:1801.09847*, 2018.
- [58] F. Dellaert, "Factor graphs and gtsam: A hands-on introduction," Georgia Institute of Technology, Tech. Rep., 2012.
- [59] W. Xu, Y. Cai, D. He, J. Lin, and F. Zhang, "Fast-lio2: Fast direct lidar-inertial odometry," *IEEE Transactions on Robotics*, 2022.
- [60] C. D. Bellicoso, M. Bjelonic, L. Wellhausen, K. Holtmann, F. Günther, M. Tranzatto, P. Fankhauser, and M. Hutter, "Advances in real-world applications for legged robots," *Journal of Field Robotics*, vol. 35, no. 8, pp. 1311–1326, 2018.
- [61] K. Koide, J. Miura, M. Yokozuka, S. Oishi, and A. Banno, "Interactive 3d graph slam for map correction," *IEEE Robotics and Automation Letters*, vol. 6, no. 1, pp. 40–47, 2020.



Jun Wu received the M.E. in control engineering from Zhejiang University, Hangzhou, China, in 2018. She is currently working toward the Ph.D. degree at the State Key Laboratory of Industrial Control Technology and Institute of Cyber-Systems and Control, Zhejiang University, Hangzhou, China. Her research interests include robotics perception.



vehicle and soft robotics.

Haojian Lu (Member, IEEE) received B.Eng. degree in Mechatronical Engineering from Beijing Institute of Technology in 2015, and he received Ph.D degree in Robotics from City University of Hong Kong in 2019. He was a Research Assistant at City University of Hong Kong, from 2019 to 2020. He is currently a professor in the State Key Laboratory of Industrial Control and Technology, and Institute of Cyber-Systems and Control, Zhejiang University. His research interests include micro/nanorobotics, bioinspired robotics, medical robotics, micro aerial



Qiuguo Zhu received his B.S. degrees in Mechanical College in 2008, and Master degrees and Doctor degree in Control Science in 2011 and 2020, respectively. He is currently an Associate Professor at Department of Control Science in Zhejiang University, Zhejiang University. His research interests include the control of humanoid robots, bipedal and quadrupedal walking and running, manipulators, rehabilitation exoskeletons and machine intelligence.



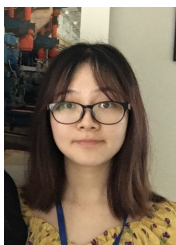
Yiyi Liao received her Ph.D. degree from the Department of Control Science and Engineering, Zhejiang University, China in 2018. From 2018 to 2021, she was a postdoctoral researcher at the Autonomous Vision Group, University of Tubingen and Max Planck Institute for Intelligent Systems, Germany. She is currently an Assistant Professor at Zhejiang University. Her research interests include 3D vision and scene understanding.



Xuecheng Xu received the B.S. degree from the Department of Control Science and Engineering, Zhejiang University, Hangzhou, P.R. China, in 2019. He is currently a Ph.D student in the College of Control Science and Engineering, Zhejiang University, Hangzhou, P.R. China. His latest research interests include LiDAR simultaneous localization and mapping and multi-robot systems.



Rong Xiong received her Ph.D. degree in Control Science and Engineering from the Department of Control Science and Engineering, Zhejiang University, Hangzhou, P.R. China in 2009. She is currently a Professor in the Department of Control Science and Engineering, Zhejiang University, Hangzhou, P.R. China. Her latest research interests include motion planning and SLAM.



Sha Lu received her B.S. from CQU-UC Joint Co-op Institute, Chongqing University, Chongqing, China, in 2021. She is currently working toward the M.S. degree at the State Key Laboratory of Industrial Control Technology and Institute of Cyber-Systems and Control, Zhejiang University, Hangzhou, China. Her research interests include robotics and deep learning.



Yue Wang (Member, IEEE) received the Ph.D. degree from the Department of Control Science and Engineering, Zhejiang University, Hangzhou, China, in 2016. He is currently working as an Associate Professor with the Department of Control Science and Engineering, Zhejiang University. His current research interests include mobile robotics and robot perception.